Monthly Notices
of the
ROYAL ASTRONOMICAL SOCIETY

MNRAS **504,** 5409–5436 (2021)
Advance Access publication 2021 April 22

doi:10.1093/mnras/stab1126

A study of cool core resiliency and entropy mixing in simulations of galaxy cluster mergers

R. Valdarnini[1,2]★ and C. L. Sarazin[3]

[1]*SISSA – Scuola Internazionale Superiore di Studi Avanzati, Via Bonomea 265, I-34136 Trieste, Italy*
[2]*INFN – Iniziativa Specifica QGSKY, Via Valerio 2, I-34127 Trieste, Italy*
[3]*Department of Astronomy, University of Virginia, 530 McCormick Road, Charlottesville, VA 22904-4325, USA*

Accepted 2021 April 13. Received 2021 March 23; in original form 2020 November 30

ABSTRACT

We present results from a suite of binary merging cluster simulations. The hydrodynamical cluster simulations are performed employing a smoothed particle hydrodynamics formulation in which gradient errors are strongly reduced by means of an integral approach. We consider adiabatic as well as radiative simulations, in which we include gas cooling, star formation, and energy feedback from supernovae. We explore the effects of merging on the thermodynamic structure of the intracluster gas of the final merger remnant. In particular, we study how core entropy is generated during the merging and the stability properties of the initial cool-core profile against disruption. To this end, we consider a range of initial mass ratio and impact parameters. Final entropy profiles of our adiabatic merging simulations are in good accord with previous findings, with cool-cores being disrupted for all of the initial merging setups. For equal-mass off-axis mergers, we find that a significant contribution to the final primary core entropy is due to hydrodynamic instabilities generated by rotational motions, which are induced by tidal torques during the first pericentre passage. In radiative simulations, cool-cores are more resilient against heating processes; none the less, they are able to maintain their integrity only in the case of off-axis mergers with very unequal masses. We suggest that these results are robust against changes in the gas physical modelling, in particular to the inclusion of AGN thermal feedback.

Our findings support the view that the observed core cluster morphology emerges naturally in a merging cluster context, and conclude that the merging angular momentum is a key parameter in shaping the thermodynamical properties of the final merger remnant.

Key words: hydrodynamics – methods: numerical – galaxies: clusters: general – galaxies: clusters: intracluster medium – X-rays: galaxies: clusters.

1 INTRODUCTION

According to the hierarchical scenario, the formation of structure in the Universe proceeds under the action of gravity through merging and accretion of smaller structures. In this framework, clusters of galaxies are the latest and most massive objects to be formed, with virial masses in the range $M \sim 10^{14} - 10^{15}\,\mathrm{M}_{\odot}$ (Voit 2005).

During their formation process, the gas is heated by adiabatic compression and shock-heating to higher temperatures. At virial equilibrium, about ∼90 per cent of the baryons in a cluster will reside in the form of an hot, X-ray emitting intracluster medium (ICM) at temperatures $T \sim 10^{7} - 10^{8}$ K.

Therefore, X-ray observations of the ICM provide X-ray maps with which to probe the spatial distribution of the cluster gas density, temperature, and metallicities. Assuming hydrostatic equilibrium and spherical symmetry, these data can then be used to deduce the underlying dark matter (DM) distribution and to determine cluster virial masses.

An accurate determination of cluster masses is necessary in order to exploit the usefulness of clusters as cosmological probes, since at any given epoch their number density is a sensitive function of the background cosmological model. This requires the clusters to be dynamically relaxed, since otherwise cluster mass estimates will be prone to uncertainties.

However, there is a large variety of observations indicating that galaxy clusters can be broadly classified into two categories: relaxed and unrelaxed (see Buote 2002, for a review). The fraction of clusters exhibiting a disturbed morphology grows with redshift and at the present epoch can be even greater than ∼50 per cent, depending on the adopted criterion used to measure the amount of substructure present in the cluster (Buote 2002). It is then fundamental to study the physics of cluster merging, not only in order to assess the status of the cluster dynamical equilibrium, but because merging between substructures (or clusters themself) gives raise to a number of interesting physical processes (Sarazin 2002; Molnar 2016).

During the merging process, collisions between substructures drive shocks into the ICM, heating the gas and injecting turbulent motions. These X-ray shocks will boost X-ray luminosities, and leave a number of observational signatures in the ICM, such as contact discontinuities (or cold fronts) in the gas temperature, radio relics, relativistic electrons, and other features (Markevitch & Vikhlinin 2007; Feretti et al. 2012).

★ E-mail: valda@sissa.it

Following the gas compression, mergers between clusters are also expected to drive star formation (Roettiger, Burns & Loken 1996; Fujita et al. 1999; Roediger et al. 2014), but with observations producing conflicting results. Some authors claim an increase in the star formation activity during mergers (Bekki, Owers & Couch 2010; Stroe et al. 2017), while it is absent in other merging systems (Mansheim et al. 2017).

Moreover, major cluster mergers are the most energetic events since the Big-Bang, with energies $\gtrsim 10^{64}$ ergs. This renders these objects unique laboratories with which to study dark matter models. Because of the collision-less nature of dark matter (DM), the position of gas and DM centres will be offset during a merging process. By contrasting X-ray and weak lensing data, it is possible to derive upper limits on the cross-section of self-interacting DM (Molnar 2016, and references cited therein). From the Bullet cluster, Markevitch et al. (2004) were the first to put an upper limit of the order of $\sigma_{\rm DM}/m_{\rm DM} \lesssim 1\,{\rm cm}^2\,{\rm g}^{-1}$ on the DM cross-section per unit mass.

Given the variety of physical phenomena and their non-linearity, *N*-body/hydrodynamical simulations are an indispensable tool with which to study merging of galaxy clusters. Numerical simulations aimed at studying cluster mergers have been performed either in a cosmological framework (Burns et al. 2008; Planelles & Quilis 2009; Rasia et al. 2015; Hahn et al. 2017; Barnes et al. 2018), or by studying the collision between two clusters in isolation. The binary merger simulations are implemented by first constructing two isolated gas+DM haloes at equilibrium, and then the initial orbital trajectory is given by assigning initial positions and velocities to the two haloes.

This method has the advantage that it allows the detailed study of a single merging event. It also simplifies the interpretation of the simulation results because the initial conditions are kept under control and the simulation can be contrasted with a specific observation. This approach has been followed by many authors (Roettiger et al. 1996; Ricker & Sarazin 2001; Ritchie & Thomas 2002; Poole et al. 2006; McCarthy et al. 2007; Poole et al. 2008; Mitchell et al. 2009; Donnert et al. 2017).

Specifically, idealized binary cluster mergers have been used to study the merging configuration of the 'Bullett cluster' (Springel & Farrar 2007; Mastropietro & Burkert 2008), as well as that of 'El Gordo' cluster (Zhang, Yu & Lu 2015, 2018) and of other merging clusters (Machado & Lima Neto 2013; Molnar & Broadhurst 2018; Halbesma et al. 2019).

Simulated X-ray maps can be constructed to study cluster merging, for instance by assessing the degree of relaxation of a specific system (ZuHone et al. 2009). Moreover, the measured offset between X-ray and Sunyaev–Zel'dovich (SZ) maps allows the relative velocity of the two merging clusters to be determined (Molnar, Hearn & Stadel 2012; Zhang, Yu & Lu 2014). These limits in turn can be used to derive constraints on the assumed cosmological model.

Another important topic in which mergers of galaxy clusters play an important role is in the study of DM properties. As previously outlined, major mergers are very energetic events in which a self-interacting DM (SIDM) is expected to exhibit significant signatures. For this reason, merging simulations with an SIDM have been carried out by many authors (Kim, Peter & Wittman 2017; Robertson, Massey & Eke 2017; ZuHone, Zavala & Vogelsberger 2019), the simulations being aimed at investigating the impact of an SIDM on gas and DM properties of the merged clusters.

Finally, numerical simulations of merging clusters have been widely used to study the origin of the observed central properties of the cluster gas. X-ray cluster surveys show that clusters can be divided into two categories according to ICM central properties (Cavagnolo et al. 2009; Johnson, Ponman & Finoguenov 2009; Pratt et al. 2010; McDonald et al. 2013): cool-core (CC) and non-cool core (NCC) clusters. CC clusters are characterized by a peaked X-ray emission, very short cooling times (∼10 per cent of the Hubble time), central temperatures about ∼1/3 of the virial ones, and radial entropy profiles steeper in the core than those of NCCs (Cavagnolo et al. 2009).

These short cooling times should induce a run-away cooling process that is not observed; to balance radiative losses, some heating sources must be operating in the cluster cores. This is the so-called 'cooling flow' problem and various heating models have been proposed in the literature to offset cooling and regulate the cooling flow (see Soker 2016, and references cited therein).

To observationally define a CC cluster, there are various criteria (Barnes et al. 2018), which depend on the available data. However, there is some consensus that CC clusters are correlated with a regular X-ray morphology (Chon, Böhringer & Smith 2012), while this is not true for NCC clusters. The latter are often associated with a disturbed morphology (Pratt et al. 2010) and exhibit a much flatter radial entropy profile than CC clusters.

These findings strongly suggest that the CC/NCC dichotomy can be naturally interpreted in terms of the cluster merging histories. In this framework, the population of NCC clusters originates as a consequence of major mergers that disrupt CC clusters. Conversely, the original core morphology is preserved for relaxed clusters that have not experienced a major merger recently.

This scenario is an important issue for a better understanding of cluster formation and evolution, and *N*-body/hydro simulations of merging clusters have been widely employed (Gómez et al. 2002; Ritchie & Thomas 2002; McCarthy et al. 2007; Burns et al. 2008; Poole et al. 2008; Planelles & Quilis 2009; ZuHone 2011; Rasia et al. 2015; Hahn et al. 2017; Barnes et al. 2018) to address the survival of CCs during cluster mergers.

Gómez et al. (2002) used 2D idealized radiative merging simulations to conclude that CCs do not survive major head-on mergers. Similar conclusions were reached for equal-mass mergers by Ritchie & Thomas (2002) and Poole et al. (2008), but from their simulations the authors argue that CCs are resilient to unequal-mass mergers if they are off-centre.

These findings are in contrast with those of ZuHone (2011). From a suite of idealized merging simulations, performed over a range of different mass ratios and impact parameters, the author finds that there is a significant degree of gas mixing taking place during the mergings. This in turn leads to higher levels of final entropy in the merger remnants and to CC disruption. Similar results were also obtained by Mitchell et al. (2009).

This discrepancy with previous simulations (Ritchie & Thomas 2002; Poole et al. 2008) could be due to a number of causes, both physical and numerical. For instance, both of the earlier authors performed their merging simulations using standard smoothed particle hydrodynamics (SPH), while Mitchell et al. (2009) and ZuHone (2011) employed the adaptive Eulerian mesh code FLASH. In terms of code capability to model fluid instabilities and gas mixing this could be a critical issue (see Section 2.3). Moreover, the simulations of Ritchie & Thomas (2002) and Poole et al. (2008) incorporated radiative cooling, while the mesh runs were adiabatic.

Early cosmological simulations (Burns et al. 2008; Planelles & Quilis 2009) have shown that there is a significant connection between the presence of CCs and the cluster merging history. In particular, Burns et al. (2008) using cosmological simulations that included cooling as well as star formation and supernovae feedback, found that CCs are resilient to late-time mergers. More recently, Rasia et al. (2015) argued that CCs can be destroyed during late-time

mergers, with active galactic nucleus (AGN) feedback playing a key role in reducing overcooling and allowing CCs to be disrupted. This is in contrast with the findings of Hahn et al. (2017), for whom the low entropy levels exhibited by simulated CCs cannot be alleviated by AGN feedback. According to Hahn et al. (2017), CC disruption depends critically on the angular momentum of the merger.

Motivated by these considerations, we present in this paper a suite of hydrodynamical simulations of merger clusters, aimed at investigating the resiliency of CCs to cluster mergers. We perform a set of *N*-body/hydrodynamical binary cluster merger simulations, with initial conditions spanning a wide range of mass ratio and impact parameters.

We use an SPH code (see Price 2012, for a review), based on a improved numerical scheme (see below). In a battery of hydrodynamical tests (Valdarnini 2016, hereafter V16), it has been demonstrated that this code can be profitably used in many astrophysical problems, without the shortcomings present in standard SPH. We perform both adiabatic and radiative merger simulations, with the latters incorporating radiative cooling as well as star formation and energy feedback from supernovae.

The initial conditions of our idealized merger simulations are set up as follows. For an isolated spherical halo composed of gas and DM initially in equilibrium, we specify the radial DM density and gas entropy profiles. To define halo parameters, we use a ΛCDM cosmology, with $\Omega_m = 0.3$, $H_0 = 70\,\mathrm{km\,s^{-1}\,Mpc^{-1}}$, and a baryon fraction of $f_b = \Omega_b/\Omega_m = 0.162$. For each of the gas and DM components, a particle realization of positions and velocities is then constructed, according to profiles computed under the assumption of hydrostatic equilibrium.

This procedure is used to construct both a primary and a secondary cluster, the virial mass of the two being related by the merging mass ratio. To initialize the merger simulation, the particle positions and velocities of the two haloes are then shifted according to the initial orbital trajectory.

Our initial condition set up is analogous to that implemented by ZuHone (2011) in his adiabatic merger simulation study. In particular, we adopt the same range of collision parameters. In this study, we have purposely chosen to adopt similar initial settings. This is in order to compare with previous results on the effects of mergers on final CC properties, specifically when cooling is included in the simulations.

Moreover, the merger simulations of ZuHone (2011) were performed using an adaptive mesh-based Eulerian code. For adiabatic simulations, it is then interesting to compare the entropy profiles of the final merger remnants against the corresponding ones presented in ZuHone (2011). This is because the two sets of simulations have been constructed by adopting very similar initial conditions, but the codes used to perform the simulations are based on two completely different numerical hydrodynamical schemes.

Our paper is organized as follows. In Section 2, we describe our hydrodynamical scheme, together with the method we use to initialize haloes in equilibrium and the orbital properties. Section 3 is dedicated to the presentation of the results, in which we describe our findings from adiabatic and radiative simulations; a specific section being dedicated to investigate the generation of entropy through mixing and shock-heating processes during the various merging phases. Finally, our main conclusions are summarized in Section 4.

2 SIMULATIONS

The simulations are performed by employing an entropy conserving SPH formulation (Price 2012). To estimate first-order SPH derivatives, the numerical scheme is improved by using an Integral Approximation (IA) accompanied by a matrix inversion, thus strongly reducing gradient errors in the momentum equation.

The IA scheme was originally proposed by García-Senz, Cabezón & Escartín (2012), and further tested in a variety of hydrodynamical tests (García-Senz et al. 2012; Rosswog 2015; V16). The results of the tests demonstrate that the new SPH formulation outperforms standard SPH and, in terms of accuracy, can be considered competitive with other numerical hydrodynamic schemes (V16). In particular, with respect to standard SPH, it is found that the IA scheme greatly improves the numerical modelling of subsonic turbulence (V16; Valdarnini 2019). This aspect is particularly important for the simulations presented here, in which a significant amount of turbulence is expected to be injected into the ICM during cluster collisions (Schmidt et al. 2017).

We now outline the basic features of the hydrodynamical method – we refer the reader to García-Senz et al. (2012) and V16 for a comprehensive description of the IA method applied to SPH. In what follows, we will refer to the SPH scheme described here as integral SPH (ISPH).

2.1 Numerical method

In SPH, the fluid is described by a set of N particles with mass m_i, velocity $\boldsymbol{v}_i$, density ρ_i , and specific entropy parameter A_i.[1] The latter is related to the particle pressure by $P_i = A_i\rho_i^{\gamma} = (\gamma - 1)\rho_i u_i$, where $\gamma = 5/3$ and u_i is the thermal energy per unit mass u_i.

At the particle position $\boldsymbol{r}_i$, the SPH gas density ρ_i is given by the summation

$$\rho_i = \sum_j m_j W(|\boldsymbol{r}_{ij}|, h_i), \tag{1}$$

where the sum is over neighbouring particles j, and $W(|\boldsymbol{r}_{ij}|, h_i)$ is a kernel with compact support. We define $W_{ij}(h_i) \equiv W(|\boldsymbol{r}_{ij}|, h_i)$. For the simulations presented here, we use the M_4 kernel (Price 2012), which is zero for $|\boldsymbol{r}_i - \boldsymbol{r}_j| \geq 2h_i$.

In equation (1), the sum is over a finite number of particles N_{nn}, and the smoothing length h_i is implicitly defined by the equation

$$\frac{4\pi(2h_i)^3\rho_i}{3} = N_{nn}m_i, \tag{2}$$

which is solved iteratively for each particle by setting $N_{nn} = 33$.

The SPH momentum equation in the IA framework reads

$$\frac{\mathrm{d}\mathbf{v}_{i,\alpha}}{\mathrm{d}t} = -\sum_j m_j \left[\frac{P_i}{\Omega_i\rho_i^2}\mathcal{A}_{\alpha,ij}(h_i) + \frac{P_j}{\Omega_j\rho_j^2}\widetilde{\mathcal{A}}_{\alpha,ij}(h_j)\right], \tag{3}$$

where Ω_i is defined as

$$\Omega_i = \left[1 - \frac{\partial h_i}{\partial\rho_i}\sum_k m_k\frac{\partial W_{ik}(h_i)}{\partial h_i}\right], \tag{4}$$

and the two terms $\mathcal{A}_{\alpha,ij}(h_i)$ and $\widetilde{\mathcal{A}}_{\alpha,ij}(h_j)$ are the IA generalization to the SPH derivatives $\nabla_i W_{ij}(h_i)$ and $\nabla_i W_{ij}(h_j)$, respectively.

These IA terms are given by

$$\mathcal{A}_{\alpha,ij}(h_i) = \sum_\beta \mathcal{C}_{\alpha\beta}(i)\Delta_\beta^{ji} W(r_{ij}, h_i),$$
$$\widetilde{\mathcal{A}}_{\alpha,ij}(h_j) = \sum_\beta \mathcal{C}_{\alpha\beta}(j)\Delta_\beta^{ji} W(r_{ij}, h_j). \tag{5}$$

[1] We use the convention of using Latin indices to denote particles and Greek indices to denote the three spatial dimensions.

Here $\Delta_\alpha^{ji} = (\mathbf{r}^j - \mathbf{r}^i)_\alpha$ and $\mathcal{C}_{\alpha\beta}(i)$ are the elements of the matrix $\mathcal{C} = \mathcal{T}^{-1}$ associated with the particle i. The inverse of this matrix is a 3×3 symmetric tensor $\mathcal{T}$, which for particle i takes the form

$$\mathcal{T}_{\alpha\beta}(i) = \sum_j \frac{m_j}{\rho_j} \Delta_\alpha^{ji} \Delta_\beta^{ji} W(r_{ij}, h_i). \tag{6}$$

To properly handle shocks, the SPH momentum equation (3) must be generalized to include an artificial viscosity (AV) term:

$$\frac{\mathrm{d}\mathbf{v}_{i,\alpha}}{\mathrm{d}t} = -\sum_j m_j \Pi_{ij} \bar{\mathcal{A}}_{\alpha,ij}, \tag{7}$$

where Π_{ij} is the AV tensor and

$$\bar{\mathcal{A}}_{\alpha,ij} = \frac{1}{2}[\mathcal{A}_{\alpha,ij}(h_i) + \mathcal{A}_{\alpha,ij}(h_j)]. \tag{8}$$

We adopt here the Riemann-based formulation proposed by Monaghan (1997) to write the AV tensor as

$$\Pi_{ij} = -\frac{\alpha_{ij}}{2} \frac{v_{ij}^{AV} \mu_{ij}}{\rho_{ij}} f_{ij}, \tag{9}$$

where $\mu_{ij} = \mathbf{v}_{ij} \cdot \mathbf{r}_{ij}/|r_{ij}|$ if $\mathbf{v}_{ij} \cdot \mathbf{r}_{ij} < 0$ but zero otherwise, $\mathbf{v}_{ij} = \mathbf{v}_i - \mathbf{v}_j$, ρ_{ij} is the arithmetic mean of the two densities and $\alpha_{ij} = (\alpha_i + \alpha_j)/2$ is the symmetrized AV parameter. The signal velocity v_{ij}^{AV} is estimated as

$$v_{ij}^{AV} = c_i + c_j - 3\mu_{ij}, \tag{10}$$

with c_i being the sound velocity. The symmetrized AV limiter $f_{ij} = (f_i + f_j)/2$, where

$$f_i = \frac{|\nabla \cdot \mathbf{v}|_\mathbf{i}}{|\nabla \cdot \mathbf{v}|_\mathbf{i} + |\nabla \times \mathbf{v}|_\mathbf{i}}, \tag{11}$$

is introduced (Balsara 1995) to suppress AV when in presence of strong shear flows. The individual particle viscosity parameters $\alpha_i(t)$ are allowed to evolve in time according the Cullen & Dehnen (2010) scheme, which is found to significantly reduce AV away from shocks [Cullen & Dehnen 2010; V16: see equation (9) and following text]. The α_i's can vary from a minimum value $\alpha_{\min} = 0.01$ when shocks are absent, up to a maximum value $\alpha_{\max} = 1.5$.

2.1.1 *Dissipative terms*

In SPH, the particle entropy A_i is generated at a rate

$$\frac{\mathrm{d}A_i}{\mathrm{d}t} = \frac{\gamma - 1}{\rho_i^{\gamma-1}}(Q_{AV} + Q_{AC} - Q_R), \tag{12}$$

where the Q_{AV} term refers to numerical viscosity effects (V16). Q_{AC} is an artificial conduction (AC) term and Q_R describes the effects of radiative cooling. The latter is defined as $Q_R = \Lambda(\rho_i, T_i, Z_i)/\rho_i$, with $\Lambda(\rho_i, T_i, Z_i)$ being the cooling function, T_i and Z_i the particle temperature and metallicity, respectively. Thus, Q_R is the cooling rate per unit mass.

The presence of the AC term is necessary in SPH simulations (Price 2008) for treating contact discontinuities, such as when studying the growth of Kelvin–Helmholtz instabilities. This term can be written as

$$\left(\frac{\mathrm{d}u_i}{\mathrm{d}t}\right)_{AC} = \sum_j \sum_\alpha \frac{m_j v_{ij}^{AC}}{\rho_{ij}} \left[\alpha_{ij}^C (u_i - u_j)\right] \Delta_\alpha^{ij} \bar{\mathcal{A}}_{\alpha,ij}/r_{ij}, \tag{13}$$

where v_{ij}^{AC} is the AC signal velocity, α_i^C is an AC parameter of the order of unity and $\alpha_{ij}^C = (\alpha_i^C + \alpha_j^C)/2$ its symmetrized value.

The form of the AC signal velocity depends on the problem under consideration (Price et al. 2018). An appropriate choice in the presence of self-gravity is found to be (Wadsley, Veeravalli & Couchman 2008; Valdarnini 2012)

$$v_{ij}^{AC} = |(\mathbf{v_i} - \mathbf{v_j}) \cdot \mathbf{r_{ij}}|/\mathbf{r_{ij}}, \tag{14}$$

which has been checked in several test cases (Valdarnini 2012) and is zero for a self-gravitating system at equilibrium.

The time evolution of the AC parameter α_i^C is regulated by a source term which is proportional to the Laplacian of the particle thermal energy, and by a decaying term which quickly damps α_i^C away from discontinuities. A description of the AC numerical settings is given in Valdarnini (2012).

Finally it is worth noting that incorporating an AC term into the SPH thermal equation significantly improves a major shortcoming of classic SPH. It is well-known (Mitchell et al. 2009) that the level of core entropies, found in non-radiative standard SPH simulations of galaxy clusters, are well below those produced in similar simulations using mesh-based codes. This difficulty is due to the Lagrangian nature of SPH, in which subgrid diffusion processes are missed. It is shown that introducing an AC term (Wadsley et al. 2008; Valdarnini 2012), the levels of entropies found in galaxy cluster cores are in much better agreement with those produced using mesh codes.

The Q_R term is present in those runs for which radiative cooling is also included. For these simulations, the gas physical modelling incorporates star formation and energy feedback from supernovae as well. For the numerical aspects of the cooling implementation, we refer to Valdarnini (2006).

2.2 Initial condition setup

For a variety of initial conditions, we perform N-body/hydrodynamical ISPH simulations to study the collisions between galaxy clusters. Each cluster consists of an isolated spherical halo initially in equilibrium, composed of dark matter and gas particles. The initial conditions of our idealized binary cluster mergers are very similar, but not identical, to those of ZuHone (2011, hereafter Z11). We study collisions between a primary and a secondary cluster, with the primary mass always set to $M_{200} = 6 \times 10^{14}\,\mathrm{M}_\odot \equiv \mathrm{M}_1$. Here M_{200} is the cluster mass within the radius r_{200}. We define r_Δ as the radius at which the cluster mean density is Δ times the cosmological critical density $\rho_c(z)$:

$$M_\Delta = \frac{4\pi}{3} \Delta \rho_c(z) r_\Delta^3. \tag{15}$$

In the following, we assume $z = 0$ as the redshift at which r_{200} is calculated. For the secondary, with cluster mass $M_{200} \equiv M_2$, we consider three different mass ratios $R = M_2/M_1 = 1{:}1$, $1{:}3$, and $1{:}10$.

For each collision with mass ratio R, we consider three different impact parameters b: a head-on cluster collision with $b = 0$, and two off-axis mergers with $b/r_{200} = 0.3$ and 0.6. Here b is the impact parameter of the collision when the distance d_{12} between the centre of mass of the two clusters is $d_{12} = r_{200}^1 + r_{200}^2$; see fig. 1 of Z11 for a geometric description of the collision set up. The procedure we use to assign initial separations and relative velocities between the two clusters is described in Section 2.2.3.

2.2.1 *Dark matter haloes*

We assume spherical symmetry for the initial dark matter (DM) and gas mass distribution. For the DM density, we adopt an NFW profile

(Navarro, Frenk & White 1997)

$$\rho_{\rm DM}(r) = \frac{\rho_s}{r/r_s(1+r/r_s)^2}\,,\ 0 \le r \le r_{200}\,, \tag{16}$$

where $c_{200} = r_{200}/r_s$ is the concentration parameter. To avoid a divergent total mass, outside r_{200} the DM density profile is suppressed exponentially (Kazantzidis, Magorrian & Moore 2004) up to a final radius $r_{\rm max} = \xi r_{200}$:

$$\rho_{\rm DM}(r) = \rho_{\rm DM}(r_{200})(r/r_{200})^{\delta} \exp -\left(\frac{r-r_{200}}{r_{\rm decay}}\right),$$
$$r_{200} < r < r_{\rm max}, \tag{17}$$

where $r_{\rm decay} = \eta r_{200}$ is the truncation radius, and the parameter δ is set by requiring the first derivative of the DM density profile to be continuous at $r = r_{200}$

$$\delta = -\frac{r_s + 3r_{200}}{r_s + r_{200}} + \frac{r_{200}}{r_{\rm decay}}. \tag{18}$$

For the runs presented here, we set the truncation parameters to the values $(\xi, \eta) = (2, 0.2)$; this choice will be motivated in Section 2.3. For a cluster of given mass, the density profile is then specified by the parameter c_{200}. For our two test clusters with $M_{200} > 10^{14}\,{\rm M}_\odot$, we set the value of c_{200} using the CLASH $c - M$ relation of Groener, Goldberg & Sereno (2016)

$$c_{200} \simeq 3.66/(M_{200}/M_\star)^{0.32}, \tag{19}$$

where $M_\star = 8 \times 10^{14}\,{\rm M}_\odot{\rm h}^{-1}$. For the cluster $C3$ with $M_{200} < 10^{14}\,{\rm M}_\odot$ we set $c_{200} = 7.03$. This value is obtained by using the following $c_{500} - M_{500}$ relation for galaxy groups (Gastaldello et al. 2007; Sun et al. 2009)

$$c_{500} = 3.96/(M_{500}/10^{14}\,{\rm M}_\odot)^{0.226}, \tag{20}$$

and solving numerically the halo profile to obtain c_{200}. Table 1 lists several initial parameters of the three idealized clusters we use to construct our simulation suite.

A numerical realization of the DM density profile is then constructed by first evaluating the enclosed DM mass $M_{\rm DM}(< r)$ within the radius r, which is normalized so that it is equal to $(1 - f_b)M_{200}$ at r_{200}. We subsequently invert $q(r) = M_{\rm DM}(< r)/M_{\rm DM}(< r_{\rm rmax}) = y$, where y is a uniform random number in the interval [0,1], to obtain the radial particle coordinate r. Finally, Cartesian coordinates are assigned to the particle by randomly orienting the particle position vector $\boldsymbol{r}$.

Kazantzidis et al. (2004) showed that, for exponentially truncated NFW haloes, particle velocities are accurately determined if their energies are drawn from the system distribution function $f(\mathcal{E})$. For spherical symmetric systems

$$\rho_h(r) = 4\pi \int_0^{\Psi(r)} f(\mathcal{E})\sqrt{2[\Psi(r) - \mathcal{E}]}\,{\rm d}\mathcal{E}, \tag{21}$$

where $\Psi(r) = -\Phi(r) = -(\Phi_h + \Phi_g)$ is the relative gravitational potential and $\mathcal{E} = \Psi - v^2/2$ is the relative energy. Here the subscripts h and g denote the DM and gas components, respectively.

Equation (21) can be inverted (Binney & Tremaine 1987) to give

$$f(\mathcal{E}) = \frac{1}{\sqrt{8}\pi^2}\left[\int_0^{\mathcal{E}} \frac{{\rm d}^2\rho_h}{{\rm d}\Psi^2}\frac{{\rm d}\Psi}{\sqrt{(\mathcal{E}-\Psi)}} + \frac{1}{\sqrt{\mathcal{E}}}\left(\frac{{\rm d}\rho_h}{{\rm d}\Psi}\right)_{\Psi=0}\right]. \tag{22}$$

The boundary term on the rhs of the equation is zero for any sensible choice of $\Psi(r)$ and $\rho(r)$ (Kazantzidis et al. 2004). The second-order derivative ${\rm d}^2\rho_h/{\rm d}\Psi^2$ can be expressed as

$$\frac{{\rm d}^2\rho}{{\rm d}\Psi^2} = \left(\frac{r^2}{GM}\right)^2\left[\frac{{\rm d}^2\rho}{{\rm d}r^2} + \frac{{\rm d}\rho}{{\rm d}r}\left(\frac{2}{r} - \frac{4\pi\rho r^2}{M}\right)\right], \tag{23}$$

which has the advantage of avoiding numerical differentiation in the integral (22), since ρ is known analytically.

The function $f(\mathcal{E})$ is then evaluated numerically and its values tabulated over a grid of energies. For a given energy $\mathcal{E}$ the value of f is obtained by interpolation. For a particle at position $\boldsymbol{r}$ with energy $\mathcal{E} \in [0, \Psi(r)]$, we randomly draw pairs $(f, \mathcal{E})$ and use an acceptance–rejection method (Kuijken & Dubinski 1994; Zemp et al. 2008; Drakos, Taylor & Benson 2017) to obtain the particle speed $v = \sqrt{2[\Psi(r) - \mathcal{E}]}$. As for the particle position, the direction of the velocity vector is randomly oriented.

These prescriptions for generating DM particle distributions at equilibrium are widely used by many authors in numerical simulations of merging cluster galaxies, for which initially DM haloes are described by an exponentially truncated NFW profile. However, a major drawback of the method introduced by Kazantzidis et al. (2004) is that the second derivative ${\rm d}^2\rho_h/{\rm d}\Psi^2$ is discontinuous at $r = r_{200}$. This implies that the behaviour of the function $f(\mathcal{E})$ can become inconsistent for certain values of $r_{\rm decay}$ (Zemp et al. 2008; Drakos et al. 2017), thus compromising halo stability over cosmological time-scales. Zemp et al. (2008) recommend the choice $\eta = r_{\rm decay}/r_{200} = 0.3$; here we show in Section 2.3 that by setting $\eta = 0.2$ one can obtain sufficiently stable haloes.

2.2.2 *Baryonic haloes*

We assume hydrostatic equilibrium to construct the cluster gas initial conditions. Following Z11, we initialize gas density and temperature profiles by specifying analytically the initial cluster entropy profile. Physically, this would be best-represented by giving the specific physical entropy per particle in the gas, $s(r)$. However, both observations of the gas in clusters and previous simulations have instead utilized a related entropy parameter [written as $S(r)$ or $K(r)$]. To be consistent and allow easier comparison to observations and previous simulations, we will adopt this convention.

Thus, in the following we refer to the 'gas entropy' as this entropy parameter $S \equiv k_B T/n_e^{2/3}$, where $k_B T$ is the gas temperature in keV and n_e the electron number density. From the Sackur–Tetrode equation (Landau & Lifshitz 1980), it is easily shown that $s = (3/2)k_B \ln(S) + {\rm const.}$, where the constant is not important here. Thus, it is straightforward to convert between s and S. However, one should be aware that differences in the entropy are exaggerated by S, since it is only its logarithm that enters into the physical entropy.

CC clusters are observationally characterized (Cavagnolo et al. 2009; Pratt et al. 2010; McDonald et al. 2013; Ghirardini et al. 2019) by dense, compact cores with cooling times shorter than H_0^{-1}. A key feature of CC clusters is that of having a level of central entropy below a threshold value $\simeq$60 keV cm^2.

We then adopt for the gas entropy profile an observationally motivated (Cavagnolo et al. 2009; Pratt et al. 2010; Ghirardini et al. 2019) functional form which consists of a power-law behaviour and an entropy floor value:

$$S(r)/S_{500} = S_0 + S_1\left(\frac{r}{r_{500}}\right)^{\alpha}, \tag{24}$$

where (Ghirardini et al. 2019)

$$S_{500} \simeq 1963\left[M_{500}/(10^{15}h^{-1}\,{\rm M}_\odot)\right]^{2/3}\,{\rm keV\,cm^2}. \tag{25}$$

For a given set of parameters (S_0, S_1, α), the entropy profile is then completely specified and we numerically integrate the equations of hydrostatic equilibrium and mass continuity:

$$\frac{{\rm d}P}{{\rm d}r} = -\frac{GM_{\rm tot}(< r)}{r^2}\rho_g, \tag{26a}$$

Table 1. Initial parameters of the three test clusters used in the merging simulations.[a].

Cluster	$M_{200}(\mathrm{M}_\odot)$	$M^h_{\rm DM}(\mathrm{M}_\odot)$	c_{200}	r_{500} (Mpc)	$S_{500}(\mathrm{keVcm}^2)$	S_0	S_1	$f_{\rm gas}$
C1	6×10^{14}	6.6×10^{14}	4.5	1.15	931	5.3×10^{-3}	1.75	0.1
C2	2×10^{14}	2.2×10^{14}	6.4	0.81	466	5.3×10^{-3}	1.84	0.086
C3	6×10^{13}	6.6×10^{13}	7.0	0.54	211	6.4×10^{-3}	2.1	0.074

Note. [a]Columns from left to right: Name of the cluster model, halo mass M_{200} at the radius r_{200}, total DM halo mass $M^h_{\rm DM}$ within $r=2r_{200}$, concentration parameter c_{200}, cluster radius r_{500} at which $\Delta=500$, gas entropy S_{500} at r_{500}, gas entropy profile parameters S_0 and S_1 (see the text), and gas mass fraction $f_{\rm gas}$ at r_{500}.

$$\frac{\mathrm{d}M_g(<r)}{\mathrm{d}r}=4\pi r^2\rho_g. \tag{26b}$$

The numerical integration of these equations is found more manageable if one integrates the temperature instead of pressure. The latter can be expressed as

$$P=\frac{\rho_g k_B T}{\mu m_p}=K\rho_g^{5/3}, \tag{27}$$

where $K(r)=S(r)(\mu/\mu_e)^{2/3}/(\mu m_p)^{5/3}$ and for the mean molecular weights we assume $\mu=0.59$, $\mu_e=1.14$. Equations (26a) and (26b) now read

$$\frac{\mathrm{d}T}{\mathrm{d}\log r}=-\frac{2\mu m_p}{5k_B}\frac{GM_{\rm tot}(<r)}{r}+\frac{3}{5}T\frac{\mathrm{d}\log K}{\mathrm{d}\log r}, \tag{28a}$$

$$\frac{\mathrm{d}\log M_g}{\mathrm{d}\log r}=\frac{4\pi r^3\rho_g}{M_g(<r)}. \tag{28b}$$

To integrate these equations, it is necessary to specify two boundary conditions. Our first condition is that $r(M_g=0)=0$, whilst the second requires that the halo gas mass at $r=r_{500}$ yields a gas mass fraction $f_g^h=M_g/M_{\rm tot}$ given by the measured relation (Sun et al. 2009)

$$f_{\rm gas}=0.035h^{-3/2}(M_{500}h/7\times10^{12}\,\mathrm{M}_\odot)^{0.135}. \tag{29}$$

To construct our gas density and temperature profiles we proceed as follows. For a given set of entropy parameters (S_0, S_1, α), we initially choose an arbitrary value of $P(r=0)\equiv P_0$ which is used to compute ρ_0 and T_0. Equations (28a) and (28b) are then numerically integrated up to $r=r_{500}$, after which the value of f_g^h is contrasted with that of $f_{\rm gas}$. We iterate the whole procedure in order to bracket the value of P_0 until the quantity $|f_g^h-f_{\rm gas}|/f_{\rm gas}$ is below a certain threshold value ($\lesssim$1 per cent). When this condition is satisfied and P_0 is a root value, we propagate the solution outwards to $r_{\rm max}=2r_{200}$. This normalization procedure implies a gas mass fraction at $r=r_{200}$ that may differ from the cosmic value f_b, and therefore that may not be entirely consistent with the normalization adopted in Section 2.2.1 for the DM component, the latter making use of the cosmic gas fraction f_b to set the halo DM mass to $(1-f_b)M_{200}$ at r_{200}. However, we have verified that for all the considered haloes the difference between the two gas fractions at $r=r_{200}$ is very small (say $\lesssim$1 per cent).

The radius up to which the gas density profiles is continued beyond r_{200} coincides here with the DM truncation radius. The choice of the gas truncation radius requires some care. Setting this radius to r_{200} would imply that gas particles at the halo edge will begin to flow outwards, owing to the absence of an external pressure. This effect implies a steepening of the gas density profile and a mass leak, which can have a significant impact on the initial mass profile when the collision time-scale is large.

To avoid this mass-leaking issue, an approach commonly employed (Turner et al. 1995; Ricker & Sarazin 2001; Poole et al. 2006; McCarthy et al. 2007; Donnert 2014) consists of surrounding the gaseous halo with a low-density, dynamically negligible, confining medium. However, this procedure comes at the cost of adding a large number of SPH particles to the simulations. We choose here a different approach by extending the gaseous halo beyond r_{200} and up to a maximum radius $r_{\rm max}=2\,r_{200}$.

The shell between r_{200} and $r_{\rm max}=2\,r_{200}$ then acts as a buffer zone that is able to keep the gas particles within r_{200} confined. Clearly the edge particles at $r\simeq2\,r_{200}$ will begin to flow outwards, leading to a steepening of the density profile. This steepening can be considered unimportant as long as collisions between clusters occur on time-scales much shorter than that necessary to modify the initial gas density profile at radii $r\lesssim r_{200}$. It will be seen in Section 2.3 that these conditions are always verified for the cluster collisions we consider.

We assume $\alpha=0.93$ in equation (24) and we report in Table 1 the coefficients S_0 and S_1, together with S_{500}, for each of the three test clusters. These coefficients are the best-fitting values of the entropy profile given by Ghirardini et al. (2019) for their CC subsample of X-COP clusters (their table 3, CC entry), but increased by about a factor of $\simeq$ 30 per cent. It has been found necessary to introduce this offset in the coefficients to obtain a physical meaningful solution to equations (28a) and (28b) up to $r_{\rm max}$. This is because, using the original coefficients, it is not possible to propagate the numerical solution beyond r_{200}, the radial profile of $P(r)$ being characterized by a very steep decline with radius. As a result, at radii slightly beyond r_{200}, the pressure becomes numerically consistent with zero.

By setting $r\simeq10^{-2}\,r_{500}$, we obtain entropy core values for our test clusters of $S/S_{500}\simeq3\times10^{-2}$ from Table 1. For cluster C1, this gives $S(r=10^{-2}\,r_{500})\simeq28\,\mathrm{keV\,cm^2}$, still below the threshold value for CC clusters (Cavagnolo et al. 2009). These core values at $r\simeq10^{-2}\,r_{500}$ are in the lower portion of the observed range of entropies for CC clusters; see fig. 6 of Ghirardini et al. (2019).

Note that for cluster C3, the coefficient $S1$ has been further increased by $\simeq$ 70 per cent, with respect to the best-fitting value of 1.35 given by Ghirardini et al. (2019). This is because all of the CC clusters of the X-COP sample used by the authors have $M_{200}>6\times10^{14}\,\mathrm{M}_\odot$, whereas here cluster C3 has $M_{200}=6\times10^{13}\,\mathrm{M}_\odot$. From fig. 10 of Sun et al. (2009), it can be seen that a core entropy of $S/S_{500}\simeq3\times10^{-2}$ at $r\simeq10^{-2}r_{500}$ is well below the observed range of entropy values reported by Sun et al. (2009) for their group sample. Finally, for cluster C1 (C3) we have at $r=10\,$kpc and the entropy core value of $\simeq25\,\mathrm{keVcm^2}$ ($\simeq12\,\mathrm{keVcm^2}$), which is about 20 per cent higher than the entropy value found at the same radius for the corresponding test cluster of Z11.

Once the initial gas density and temperature profiles are computed for the range $0\le r\le r_{\rm max}$, we use them to construct the initial particle configuration. To this end, we store the profiles on a very fine grid. This is in order to obtain $\rho(r)$ and $T(r)$ at a generic radius r using grid values.

In SPH, a non-trivial issue is the realization of the gas particle distribution which must reproduce the required density profile $\rho(r)$. From equation (1), one can see that in SPH the density at a given particle position depends on the masses and relative positions of nearby particles. This in turn implies that any specific realization of particle positions which satisfies the prescribed profile $\rho(r)$, must be found by solving simultaneously for all the particle positions. This is a difficult task and several methods have been devised to solve the problem.

A relatively simple approach, which starts from a uniform distribution and solves equation (1) by varying particle masses, cannot be applied in SPH. This is because numerical instabilities are found to arise (Monaghan & Price 2006) when large mass contrasts are present between particles. Similarly, a random realization of particle positions generated from the specified $\rho(r)$, as we did in Section 2.2.1 to construct the DM particle positions, cannot be used here. The noise induced by Poisson sampling implies the development of large fluctuations which in turn quickly perturb the initial equilibrium profile.

These difficulties have lead many authors to develop alternative methods to solve the problem of properly generating initial conditions in SPH. These methods can be summarized as follows: lattice stretching (Herant 1994; Rosswog & Price 2007), viscous damping (Price & Monaghan 2007; Wang & White 2007; Pakmor et al. 2012; Price et al. 2018), relaxation (Zurek & Benz 1986; Nagasawa, Nakamura & Miyama 1988), space partition based either on tessellation (Pakmor et al. 2012; Raskin & Owen 2016; Reinhardt & Stadel 2017), or weighted Voronoi tessellations (Diehl et al. 2015; Vela, Sanchez & Geiger 2018; Arth et al. 2019).

Initially, we implemented the method of Diehl et al. (2015) to setup our SPH initial conditions. The algorithm is based on a Voronoi tessellation in which particles are moved iteratively towards a relaxed configuration. However, during the merging simulations the halo profiles constructed according to this procedure were found to deviate from the initial equilibrium solution. In several cases, this happened on a time-scale shorter than that occurring between the start of the simulation and the cluster collision.

We interpret this behaviour as a direct consequence of the entropy profile we use to construct our initial conditions. For CC clusters, the average entropy profile implies an equilibrium solution with a very steep density profile towards the cluster centre. As a result, it is intrinsically difficult to keep SPH gradient errors under control. We have indirectly verified that is the case by running a halo in isolation for several gigayears; the physical parameters of the halo were those of cluster C1. The DM and gas particle realization were constructed following the procedure just described, but the parameters of the entropy profile were the best-fitting values extracted from a subsample of simulated NCC clusters (Valdarnini 2019). In such a case, the halo gas density profile was found quite stable over the whole simulation period.

To solve this issue, we then adopt the following procedure. Initially, gas particle positions are obtained by a radial transformation applied to the coordinates of a uniform glass distribution of points. This is a minimal noise configuration, and it is generated by applying to an initial Poisson distribution of points a reversed gravitational acceleration together with a damping force (Wang & White 2007). Particle positions are advanced until a low energy state is reached.

The radial transformation is such that the new gas positions are consistent with the desired initial gas mass profile. This profile is now much more stable than that obtained from a random realization (Section 2.3), but its stability properties are not yet sufficient to consistently satisfy the initial condition set up required by the merging runs studied here.

To further improve the stability properties of the gaseous halo, we add to the momentum equation a time-dependent friction term (Price & Monaghan 2007; Pakmor et al. 2012)

$$\frac{\mathrm{d}\mathbf{v}_i}{\mathrm{d}t} = -\frac{\mathbf{v}_i - \mathbf{V}_{\rm cm}}{\tau_{\rm damp}} + \left(\frac{\mathrm{d}\mathbf{v}_i}{\mathrm{d}t}\right)_{\rm SPH}, \tag{30}$$

where the second term on the RHS is given by equation (3), $\boldsymbol{V}_{\rm cm}$ is the halo centre of mass velocity, and $\tau_{\rm damp}$ is a time-dependent damping time scale. This is written as

$$\tau_{\rm damp} = \frac{\tau_{\rm dyn}}{\alpha_{\rm damp}}, \tag{31}$$

where $\tau_{\rm dyn} = 1/\sqrt{4\pi G\rho_d}$ is the local dynamical time-scale, $\rho_d(\boldsymbol{x}_i)$ is the particle DM density, and $\alpha_{\rm damp}$ is a friction parameter which controls the strength of the friction. The DM density ρ_d must be calculated at run time according to an SPH prescription, but one can introduce a DM to gas density ratio: $\beta_{\rm dyn} = \rho_d/\rho_g$. The halo stability can then be exploited to avoid the calculation of the DM density by using $\beta_{\rm dyn}\rho_g$ in place of ρ_d in equation (31). As it will be seen from the plots of Section 2.3, a conservative value for $\beta_{\rm dyn}$ is obtained by setting $\beta_{\rm dyn} \simeq 50$. It has been found that this choice also has an impact on the value of $\alpha_{\rm damp}$. In principle, $\tau_{\rm damp}$ should be a small fraction of $\tau_{\rm dyn}$, but with the adopted value of $\beta_{\rm dyn}$ very stable haloes are already obtained when $\alpha_{\rm damp} \simeq 3$.

Our merging simulations are then performed by using the generalized momentum equation (30) as the simulations start, and switching off ($\alpha_{\rm damp} = 0$) the friction parameter at a simulation time which depends on the initial merging kinematics (Section 2.2.3). Initially, we set gas particle velocities to zero and temperatures are assigned by interpolating grid values. These are calculated from the numerical solution and the interpolation is done according to the radial particle coordinates.

Finally, we set the mass of DM and gas particles according to the scaling $m_d \simeq 8\times10^8\,\mathrm{M}_\odot(\mathrm{M}_{200}/2\times10^{14}\,\mathrm{M}_\odot)$ and $m_g = f_b m_d/(1-f_b)) \simeq 0.16 m_d$, respectively. These mass assignments are consistent with previous findings (Valdarnini 2019), in which ICM profiles extracted from a set of hydrodynamical cluster simulations were found numerically converged when similar settings were adopted for the particle masses. However, as outlined before, in SPH numerical instabilities can arise in the presence of very different gas particle masses. This implies that the simulation numerical resolution is enforced by the smallest mass of the binary system. We thus write

$$m_d \simeq 8\times10^8\,\mathrm{M}_\odot(\mathrm{M}^{(2)}_{200}/2\times10^{14}\,\mathrm{M}_\odot). \tag{32}$$

For cluster C1, the total number of gas particles ranges then from $N_g^{(1)} \simeq 2\times10^5$ when the collision mass ratio is $R = 1{:}1$, up to $N_g^{(1)} \simeq 2\times10^6$ when $R = 1{:}10$. For cluster $C3$ one has $N_g^{(2)} \simeq 1.27\times10^5$. The gravitational softening parameters of the particles are set according to the scaling $\varepsilon_i = 15.8\cdot(m_i/6.2\times10^8\,\mathrm{M}_\odot)^{1/3}$ kpc. Additionally, in some test cases we run high-resolution (HR) simulations in which the particle masses are scaled down by a factor 4, with respect to the reference value given by equation (32).

2.2.3 *Initial merger kinematics*

To construct the orbits of our merging simulations, we choose a Cartesian system of coordinates $\{x, y, z\}$, with the centre of mass of the two clusters being at the origin. The orbits are initialized in the $\{x, y\}$ plane at $z = 0$, with $\{\mathbf{d}^{in}, \mathbf{V}^{in}\}$ being the initial separation and relative velocity vectors, respectively. Thus, the initial $\{x, y\}$

coordinates of the two cluster centre of mass read $-(d_x^{in}, d_y^{in})/(1+R)$ and $(d_x^{in}, d_y^{in})R/(1+R)$. Similarly, the velocity components are given by $-(V_x^{in}, V_y^{in})/(1+R)$ and $(V_x^{in}, V_y^{in})R/(1+R)$.

As already outlined, our collision parameter space is the same as in Z11. However, there is here a significant difference in the initial condition setup of the haloes. For the reasons discussed in Sections 2.2.1 and 2.2.2, the initial DM and gas mass profiles are continued beyond r_{200} and extended up to $2r_{200}$. This implies that, unlike in Z11, the relative initial separation cannot be set here to the sum of the two virial radii, but to twice its value: $d_{\rm in} = 2(r_{200}^1 + r_{200}^2)$. As discussed in Section 2.3, this is to avoid a significant overlap at the start of the simulation between the mass profiles of the two haloes, which in turn would soon put the profiles out of equilibrium.

Our initial condition vectors $\{\mathbf{d}^{in}, \mathbf{V}^{in}\}$ at $t = 0$ must then be chosen such that, at some later simulation time t, the orbit of the binary cluster system produces the initial conditions of Z11. These consists of a separation $d_{\rm in}/2$ between the two cluster centres of mass, with a collision impact parameter b and relative infall velocity $V \simeq 1.1\sqrt{GM_{200}/r_{200}}$. The latter value is justified by cosmological simulations (Vitvitska et al. 2002).

In order to realize these settings, we adopt a procedure similar to that described in Poole et al. (2006). For a specified set of initial conditions taken from Z11, we first approximate the two clusters as point-like and accordingly assign positions and velocities to the two points. We tag this orbital status as occurring at the time t_f, i.e. the start of the Z11 simulations. We now numerically solve Kepler's problem by seeking the time $t_i < t_f$ such that the separation between the two points is $d_{\rm in}$. The orbital positions and velocities at t_i then complete the solution vectors $\{\mathbf{d}^{in}, \mathbf{V}^{in}\}$.

To account for tidal distortions, we first run a DM only merging simulation, using as initial conditions the solution vectors $\{\mathbf{d}^{in}, \mathbf{V}^{in}\}(t=0)$ previously determined. During the simulations we denote as $\{\mathbf{X}_{cl}, \mathbf{V}_{cl}\}(t)$ the centre of mass position and velocities of the two haloes. These vectors are contrasted with the Z11 initial conditions $\{\mathbf{X}_{cl}^Z, \mathbf{V}_{cl}^Z\}(\tau^K)$, which the binary system must reproduce at the simulation time $t_s = t_f - t_i \equiv \tau^K$. To quantify the deviations between the specified set of initial conditions and the numerical solution we define the following norms

$$\begin{cases} \varepsilon_x^{(cl)}(t) = \left\|\mathbf{X}_{cl}(t) - \mathbf{X}_{cl}^Z(\tau^K)\right\| \Big/ \left\|\mathbf{X}_{cl}^Z(\tau^K)\right\| \\ \varepsilon_v^{(cl)}(t) = \left\|\mathbf{V}_{cl}(t) - \mathbf{V}_{cl}^Z(\tau^K)\right\| \Big/ \left\|\mathbf{V}_{cl}^Z(\tau^K)\right\|, \end{cases} \tag{33}$$

with $cl = 1, 2$ being the halo index.

We define as position error $\varepsilon_x(t)$ the maximum of the two error norms: $\varepsilon_x(t) = MAX(\varepsilon_x^{(1)}(t), \varepsilon_x^{(2)}(t))$, the velocity error $\varepsilon_v(t)$ being similarly defined. These errors are computed and saved at run times $t_m = \tau^k + m\Delta t$, centred around τ^K. We set the grid spacing to $\Delta t = 1/16$ Gyr and m is an integer ranging between -20 and 20. Finally, the simulation time at which our constructed set of error values has a minimum, is identified as the simulation time $t = 0$ in the corresponding merging run of Z11. We label as $\tau^{\rm num}$ this solution time obtained numerically. Table 2 lists the values of $\tau^{\rm num}$ and τ^K for each of our merging runs, together with the notation we use to label the different simulations. Note that the difference $\tau^{\rm num} - \tau^K$ is smallest for head-on collisions, while it is largest ($\simeq$0.3 Gyr) for the $R = 1{:}1$ off-axis merger with $b = 0.6$. The simulation time t_s here is then related to that of Z11 by the relation:

$$t^Z = t_s - \tau^{\rm num}. \tag{34}$$

Our merging simulations are performed up to a simulation time $t_s = \tau^{\rm num} + t_{\rm fin}$, where $t_{\rm fin} = 10$ Gyr. We analyse simulation results when $t^Z \geq 0$, at epochs spaced by 1 Gyr. To ease comparisons between our results and those of Z11, hereafter we will always use the simulation time t^Z, which we abbreviate as t.

Table 2. The simulation ID is defined according to the mass ratio R and the impact parameter b of the collision, second column the corresponding ID of the Z11 runs. The simulations start at $t_s = 0$, the time $\tau^{\rm num}$ is the simulation time at which the centre of mass position and velocities of the two haloes are closest to the corresponding Z11 initial conditions. ε_x and ε_v are the corresponding relative errors, τ^K is the analytic solution given by the Kepler's problem.

ID	ID Z11	$\tau^{\rm num}$ (Gyr)	τ^K (Gyr)	ε_x	ε_v
*R*01*b*00	*S*1	3.81	3.73	1.06×10^{-2}	0.115
*R*01*b*03	*S*2	3.94	4.17	2.3×10^{-2}	0.09
*R*01*b*06	*S*3	4.81	5.10	4.1×10^{-2}	0.13
*R*03*b*00	*S*4	2.81	2.73	1.4×10^{-2}	0.09
*R*03*b*03	*S*5	2.87	2.99	1.2×10^{-2}	0.08
*R*03*b*06	*S*6	3.31	3.41	2.8×10^{-2}	0.11
*R*10*b*00	*S*7	2.32	2.32	3.7×10^{-2}	0.06
*R*10*b*03	*S*8	2.44	2.53	1.03×10^{-2}	0.08
*R*10*b*06	*S*9	2.75	2.87	2.4×10^{-2}	0.09

The damping factor $\alpha_{\rm damp}$ in equation (30) is set to zero when $t \geq 0$, but with some exceptions (see later). This guarantees that at $t = 0$ our halo entropy profiles possess the correct radial behaviour. Our merging simulation suite is constructed by performing both adiabatic and radiative simulations. For adiabatic runs, we consider all of the collision parameter space, consisting of nine different merging simulations. For radiative simulations, we run only a limited number of mergers because of the high computational cost of the simulations.

2.3 Stability tests

As already discussed in Section 2.2.1, the stability of spherically symmetric DM haloes with an exponentially truncated NFW profile depends critically on how initial particle velocities are assigned. According to Kazantzidis et al. (2004), the long-term halo evolution is significantly affected if the particle velocities are initialized using the local Maxwellian approximation. By contrast, much more stable haloes are obtained when the initial particle energies are consistently extracted from the equilibrium distribution function $f(\mathcal{E})$. However, the choice of the halo truncation parameters $\xi = r_{\rm max}/r_{200}$ and $\eta = r_{\rm decay}/r_{200}$ is not entirely arbitrary. In particular, an overly sharp truncation ($\eta \lesssim 0.1$) can lead to instabilities in the halo evolution (Zemp et al. 2008; Drakos et al. 2017). The solution is to increase the truncation radius ($\eta \simeq 0.3$), truncating the atmosphere more smoothly, as already done in some merging runs (Zhang et al. 2014).

To validate our choice of the truncation parameters (ξ, η) we studied the evolution over cosmological time-scales of three isolated DM haloes. All of the haloes have $M_{200} = 6 \times 10^{14}\,{\rm M}_\odot$, but their initial density profiles have different truncation parameters (ξ, η). The three pairs of values we consider are (ξ, η) = (3, 0.3), (1.4, 0.1), and (2, 0.2). We refer to the corresponding halo realizations as DMa, DMb, and DMc, respectively. Initial particle position and velocities are initialized according to the procedures described in Section 2.2.1, and we use equation (32) to set the DM particle mass to $m_d \simeq 2.4 \times 10^9\,{\rm M}_\odot$. The number of DM particles N_p then ranges from $N_p \simeq 3 \times 10^5$ for the DMb halo, up to $N_p \simeq 3.8 \times 10^5$ in the case of the DMa halo.

Fig. 1 shows the time evolution of the density and velocity dispersion profiles for the three haloes at four different time slices: $t = 0$, 1, 5, and 10 Gyr. For the range of initial conditions, we consider the time span $t_{\rm hit}$ occurring between the start of the simulation and the

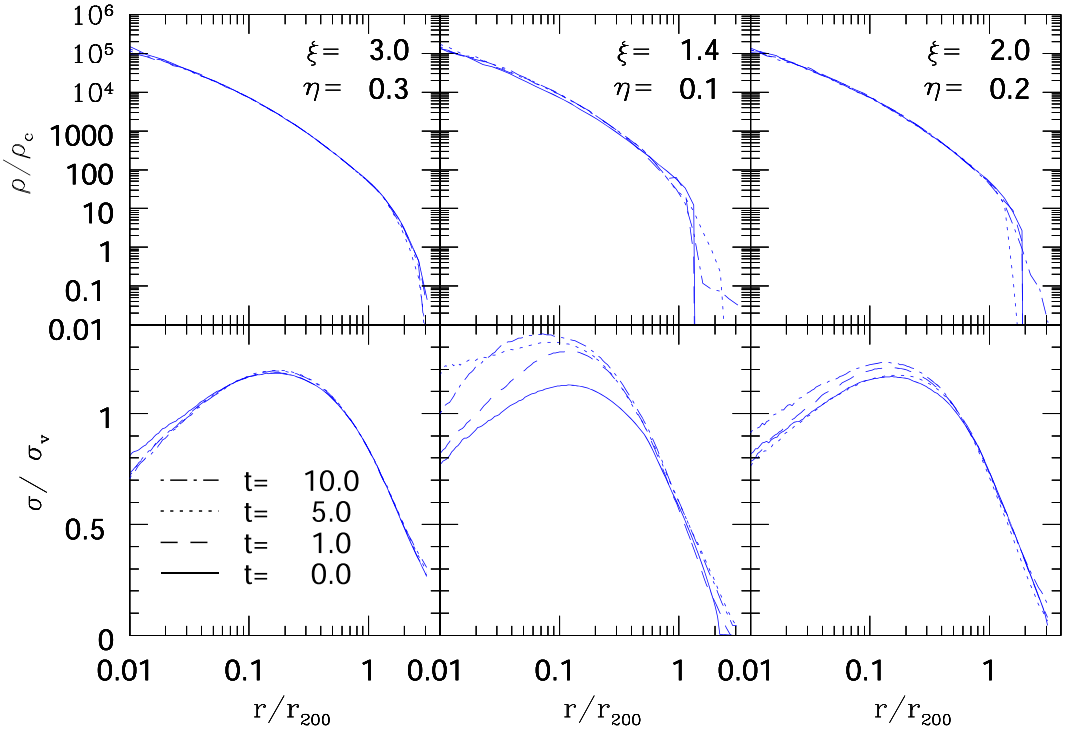

Figure 1. Evolution of the density (top panels) and velocity dispersion (bottom panels) profiles for three different isolated DM haloes (left to right). The haloes are initially in equilibrium, with the particle distributions realized according to the procedures described in Section 2.2.1. All of the haloes have $M_{200} = 6 \times 10^{14}\,\mathrm{M}_{\odot}$, but their initial conditions differ in the choice of the truncation parameters (ξ, η) (see the text). Density is in units of the cosmological critical density and velocity dispersion in units of $\sigma_{200} = \sqrt{GM_{200}/r_{200}} \equiv \sigma_v$. Different line styles refer to different epochs, as indicated in the bottom left-hand panel, where the time is in Gyr. (Note that the times decrease from top to bottom in the legend in this and subsequent figures.).

direct hit between the primary and secondary cluster cores (see later) ranges from $\simeq$Gyr, in the case of head-on collisions, up to $\simeq$8 Gyr for the *R*10*b*06 initial merging configuration. The different epochs displayed in Fig. 1 have been chosen with the criterion of covering the whole range of time spans $t_{\rm hit}$.

As it can be seen, the best stability properties are exhibited by the DMa halo. For this halo, both density and velocity dispersion profiles are quite stable up to $\simeq$10 Gyr. This is in accordance with previous findings (Zemp et al. 2008; Drakos et al. 2017), and confirms that setting $\eta = 0.3$ is the safest choice when stability is an issue. However, this choice of $r_{\rm decay}$ requires the continuation of the DM halo beyond r_{200} and up to $r_{\rm max} \simeq 3r_{200}$, if one wants to avoid an abrupt truncation in the density profile. This choice of the truncation parameters (ξ, η) in turn implies that the simulations will begin with a significant overlap between the two DM haloes, if the initial separation between the two clusters is chosen to be $d_{\rm in} = r^1_{200} + r^2_{200}$, as in Z11. These initial settings then put the initial mass profiles of the two haloes out of equilibrium, and it is not clear what the impact of these initial conditions is on ICM properties during cluster mergers (McCarthy et al. 2007).

We choose here to put the initial separation between the two cluster centre of mass to the value $d_{\rm in} = \xi(r^1_{200} + r^2_{200})$, this choice of the initial setup being clearly advantageous because the merging runs are then performed with haloes initially at equilibrium. To avoid very large values ($\gtrsim$10 Gyr) of the simulation time $\tau^{\rm num}$, when the two clusters orbital parameters best approximate the Z11 initial conditions, we decided here to use a value of ξ smaller than that of the DMa halo ($\xi = 3$).

Fig. 1 shows that the stability properties of the DMc halo, having $(\xi, \eta) = (2, 0.2)$, are much better than those of the DMb halo with $(\xi, \eta) = (1.4, 0.1)$. There is some evolution in the density profile beyond r_{200}, but the velocity dispersion profile is much more stable than those of the DMb halo. To set up initial conditions for our DM haloes, we thus adopt as truncation parameters the pair of values $(\xi, \eta) = (2, 0.2)$.

This choice is motivated by the criterion of having the DM haloes as stable as possible, but without extending them very far beyond r_{200}. It must be stressed that this choice does not necessarily imply that final gas profiles are significantly affected by using the pair $(\xi, \eta) = (1.4, 0.1)$. For instance, fig. 2 of Z11 shows little evolution in the gas profiles of an isolated halo, although the DM component is initialized by setting $\eta = 0.1$.

We now investigate the stability properties of haloes which contain both DM and gas. As for the DM-only tests, we always set the halo mass at r_{200} to $M_{200} = 6 \times 10^{14}\,\mathrm{M}_{\odot}$. We setup the gas density and temperature profiles according to the procedure described in Section 2.2.2, the entropy profile parameters being those of cluster C1. All of the haloes have then the same physical parameters and analytical profiles. The total DM and gas halo masses at $r_{\rm max} = 2r_{200}$ are then $M^h_{\rm DM} \simeq 6.6 \times 10^{14}\,\mathrm{M}_{\odot}$ and $M^h_{\rm gas} \simeq 9.2 \times 10^{13}\,\mathrm{M}_{\odot}$, respectively. Accordingly, from equation (32) the number of DM (gas) particles is $N_p \simeq 2.7 \times 10^5$ (2×10^5).

We initially consider two different particle realizations of the initial gas density profile. The first halo (RN) has gas particle positions drawn from a uniform random distribution. This is the simplest approach to realize the desired density profile, but for the reasons discussed in Section 2.2.2, the stability of its gas profiles can be considered very poor. Thus, we use the profile evolution of this halo realization as a benchmark, against which to assess the stability properties of other procedures. For the second halo (GL) gas positions are obtained by transforming the radial coordinates of a glass-like

configuration of points. The transformation is consistently done by numerically solving for the radial coordinate of each particle that satisfies the requested mass profile.

For the two-halo realizations, Fig. 2 shows the time evolution of the gas density, temperature, and entropy profiles. The temperature is in units of T_{200}, the mass-weighted temperature within r_{200}, and entropy in units of S_{500}. Additionally, we also show the radial profiles of the dynamical time in gas and the cooling time (defined in equation 35 below).

As expected, the plots clearly show the very poor stability properties of the RN halo. On the other hand, there is some improvement when using glass-like initial conditions. The entropy profile $S_{\rm GL}(r)$ exhibits a better stability, with deviations from the initial reference profile systematically smaller than in the RN case. At $t = 1$ Gyr there are small deviations in the very inner region ($r \lesssim 0.02 r_{500}$), and at $t = 10$ Gyr the profile $S_{\rm GL}(r)$ is similar to that of $S_{\rm RN}(r)$ at $t = 5$ Gyr.

These results demonstrate that in order to improve the profile stability of our SPH particle realization, one must resort to more sophisticated methods. As outlined in Section 2.2.2, the use of a relaxation method (Diehl et al. 2015) was found to improve the profile stability, but not in a very significant way with respect to the GL run. Motivated by previous findings (Price & Monaghan 2007; Pakmor et al. 2012), in order to keep the initial configuration in equilibrium we then add a time-dependent damping force to the SPH momentum equation. The procedure and the parameter settings are described in the previous section.

For this test case, which we label as FD, Fig. 3 shows the time evolution of the different gas profiles. The meaning of the different panels and lines being the same of Fig. 2. The profile evolution clearly indicates that the damping method is very good in maintaining the stability of the initial SPH particle realization, and in turn the gas profiles. We have verified that this behaviour holds for clusters C2 and C3 as well.

Accordingly, we implement this setup procedure to construct stable gas profiles. The initial particle positions are extracted from a uniform glass-like distribution, as for the GL halo. The hydrodynamic SPH force equation is then generalized in equation (30) to incorporate a friction term. The latter is present from the start of the simulation ($t_s = 0$) up to the time when the binary system has reached the optimal configuration aimed at reproducing the Z11 initial conditions ($t_s = \tau^{\rm num}$). After this epoch ($t = t_s - \tau^{\rm num} \geq 0$), the friction term is switched off ($\alpha_{\rm damp} = 0$) in the momentum equation. With these settings, we can consistently compare our simulation results with those of Z11, having realized the same cluster orbital and gas profile initial conditions

However, it must be stressed that in some mergers the clusters will come in contact having higher core entropies than those initially specified. We define the time span $t_{\rm hit}$ as that occurring between the start of the simulation and when the two clusters cores collide or interact strongly. For our head-on mergers ($b = 0$), we find that this is well approximated by the epoch when the distance between the two cluster centres of mass is smaller than r^1_{200}. However, for our offset mergers with $b = 0.3$ or 0.6, we find that the secondary core passes by the primary core without being significantly affected during the first pericentric passage. After the secondary reaches the apocentre, it falls more directly into the primary core. Thus, this second encounter is nearly head-on, and we therefore apply the same definition as for $b = 0$ to this second encounter. Empirically, we find that this time-scale does approximate the time when the secondary core is significantly affected. For example, for the *R*10*b*06 merging run one has $t_{\rm hit} \simeq 8$ Gyr.

In general, we find that there is some small evolution in the inner ($r \lesssim 0.1\, r_{500}$) level of initial ($t = 0$) entropy of the primary cluster when $t_{\rm hit} \gtrsim 4$ Gyr. This shows that long-term stability in the initial profiles is not always achieved, even after the application of a friction term to the motion of the SPH particles. To assess the impact of this behaviour on the final ($t = 10$ Gyr) entropy profile of the merged clusters, we performed some of our merging simulations with the friction term still active up to $t = t_{\rm hit}$. These runs will be discussed in detail later; unless otherwise stated in the following, we will discuss merging simulations in which the friction term $\alpha_{\rm damp}$ is set to zero when $t \geq 0$.

Finally, we also show in Fig. 3 the time evolution of the different gaseous halo profiles when the SPH entropy equation (12) incorporates radiative cooling. Following Z11, we adapt the bremsstrahlung cooling time approximation:

$$\tau_c \simeq 28.7\,{\rm Gyr} \left(\frac{S}{100\,{\rm keV\,cm^2}} \right)^{1/2} \left(\frac{n_e}{10^{-3}\,{\rm cm^{-3}}} \right)^{-2/3}. \quad (35)$$

The test runs with radiative cooling are indicated as CR in the panels. As for the FD runs, the initial conditions are the same as for the GL halo, but here the damping term is absent in the momentum equation (30). These settings allow us to assess the impact of radiative cooling on the thermal evolution of an isolated halo initially in equilibrium. The cooling time profiles in Figs 2 and 3 show that the condition $\tau_c \gg \tau_{\rm dyn}$ is always satisfied at all radii, thus suggesting that radiative processes are not very important dynamically (e.g. motions induced by cooling will be very subsonic).

The results indicate that in the halo inner regions ($r \lesssim 0.1\, r_{500}$), radiative losses become significant on time-scales $t^h_{\rm rad} \gtrsim 5$ Gyr, in accordance with the range of cooling times $\tau_c(r)$ displayed by the CR halo in the bottom left-hand panel. From Table 2 one can see that the condition $t^h_{\rm rad} \gg \tau^{\rm num}$ is not always satisfied, this in turn implies that for some merging runs with cooling the entropy profile at $t_s = \tau^{\rm num}$ ($t = 0$) will not satisfy the prescribed initial conditions.

To construct the initial setup for the merging simulations with cooling, we then proceed as follows. The simulations are performed up to $t_s = \tau^{\rm num}$ as in the adiabatic case, with the friction term present and, in particular, the cooling term Q_R in equation (12) switched off. This guarantees that both adiabatic and radiative simulations will start at $t = 0$ with the same profiles. After this epoch, the radiative merging runs are performed with the Q_R term now present in equation (12) and the damping term switched off.

Note that the previous discussion about the appropriate level of core entropy when $t_{\rm hit}$ is large (say $\gtrsim$5 Gyr), is not relevant here. This is because the time evolution of the CR halo profiles demonstrate that core heating due to numerical effects is subdominant with respect to radiative losses.

3 RESULTS

In this section, we present our main results from the simulations we performed. We first discuss results from adiabatic simulations and subsequently those obtained from the cooling runs. Our findings are qualitatively discussed in light of the impact on the final entropy profiles of the different merging processes we consider.

3.1 Adiabatic runs

For the nine merging simulations we show in Fig. 4 the final gas density and temperature profiles of the resulting merging clusters. The plots are depicted at $t = 10$ Gyr, an elapsed time since the start of the collision which should be sufficiently large

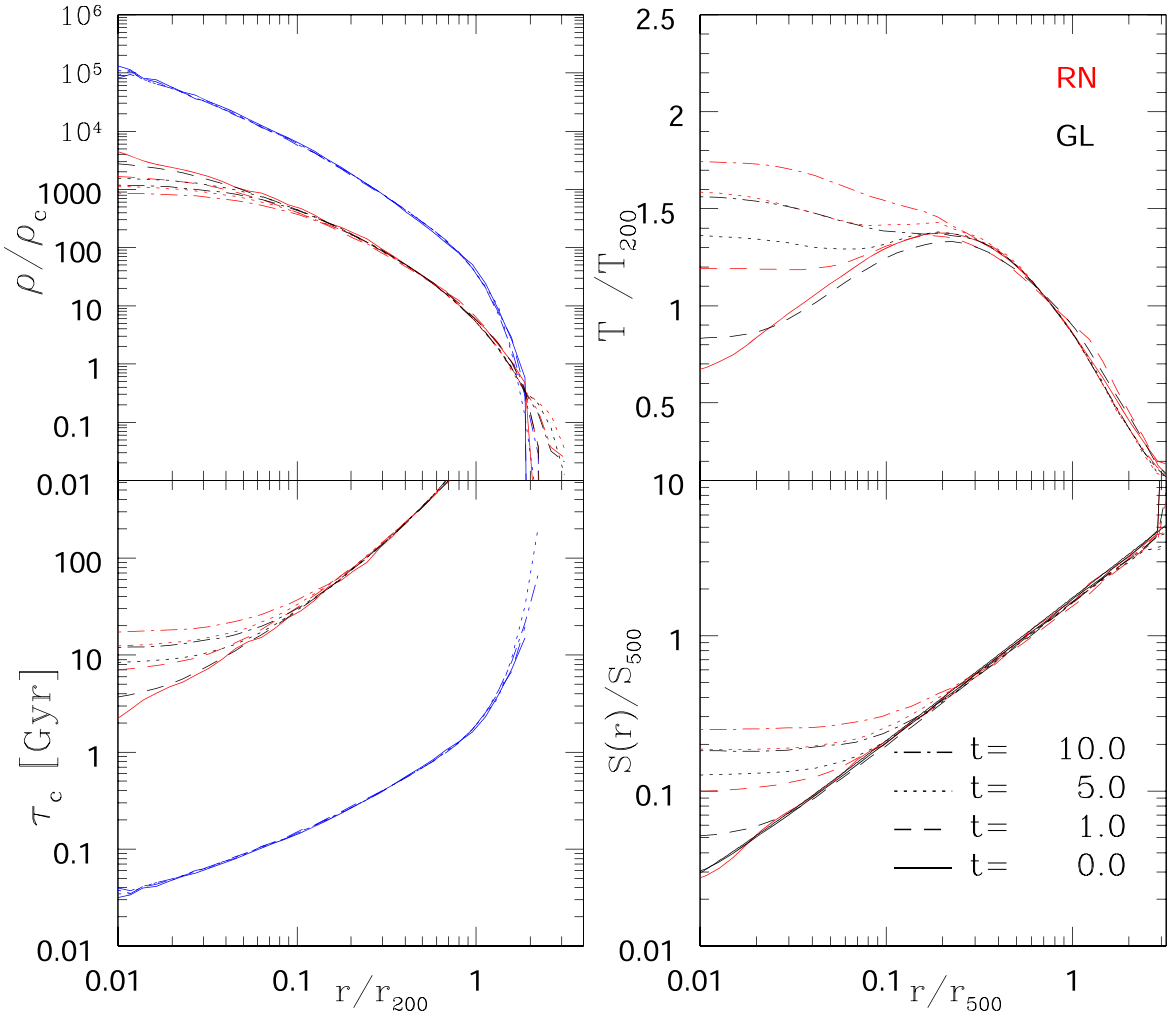

Figure 2. Time evolution of several gas profiles for two isolated gas+DM haloes. Both haloes have the same physical parameters and $M_{200} = 6 \times 10^{14}\,\mathrm{M}_{\odot}$. The initial gas density and temperature profiles are derived from the entropy profile as given by equation (24), and the parameters S_0 and S_1 are those of cluster C1 (see Table 1). From the top left going clockwise: the gas density, temperature, entropy, and cooling time τ_c (equation 35). As in Fig. 1, different line styles refer to different epochs. The two haloes differ in the realization of the gas particle distribution used to model the initial gas density profile $\rho_g^{(\mathrm{in})}(r)$. We consider an initial setup in which gas particle positions are randomly drawn (RN) to obtain $\rho_g^{(\mathrm{in})}(r)$, whilst in the other setup the gas positions are obtained by radially stretching a uniform glass point distribution (GL). In each panel, red (black) lines are for the RN (GL) run. In the left-hand panels, the blue lines refer to the halo DM density profile (top) and to the local dynamical time $\tau_{\mathrm{dyn}}(r)$ (bottom). For the sake of clarity, these profiles are shown only for the RN run. Similarly, the gas profiles of the GL halo at $t = 0$ are not depicted. Entropy is normalized to S_{500}, as given by equation (25), and T_{200} is the mass-weighted temperature within r_{200}. In the bottom right-hand panel the solid black line indicates the analytical entropy profile (24).

to guarantee a relaxed state for all of the considered merging configurations.

The radial profiles are calculated for each radial bin by spherical averaging the extensible physical quantities. These are total electron number for the average electron density, total thermal energy divided by 3/2 of the total particle number for the gas temperature, and total physical entropy (adding up the specific physical entropy per particle s for all the particles, dividing by the total number of particles, and converting to the average entropy parameter S as discussed at the start of Section 2.2.2) for the entropy parameter.

As in Z11, for each physical quantity we have subdivided the plots by showing in each panel of Fig. 4 profiles extracted from merging runs with the same mass ratio but different impact parameters. This layout is common also to the other figures, and allows a better comparison with previous findings.

The radial behaviour of the final density profiles depicted in Fig. 4 exhibit the common feature of a flattened density ($n_e \simeq 2 \times 10^{-3}\,\mathrm{cm}^{-3}$) at cluster radii $r \lesssim 300\,\mathrm{kpc}$. This flattening is in sharp contrast with the initial density profiles, which are constructed so as to reproduce that of cooling flow clusters. The initial profiles steadily increase towards the cluster centres and have much higher central densities ($n_e \simeq 2 \times 10^{-2}\,\mathrm{cm}^{-3}$).

Similarly, the final temperature profiles no longer show the initial inversion and steadily increase towards the cluster centres. There is a wide range of central temperature values, from $\simeq 5\,\mathrm{keV}$ up to $\simeq 15\,\mathrm{keV}$, depending on the mass ratio R and impact parameter b of the merging simulation.

These findings strongly suggest that the initial cool-core cluster configurations do not survive the impact on the gas of the processes that occur during the collisions. This issue is central to the paper and will be addressed later, when discussing the final entropy profiles.

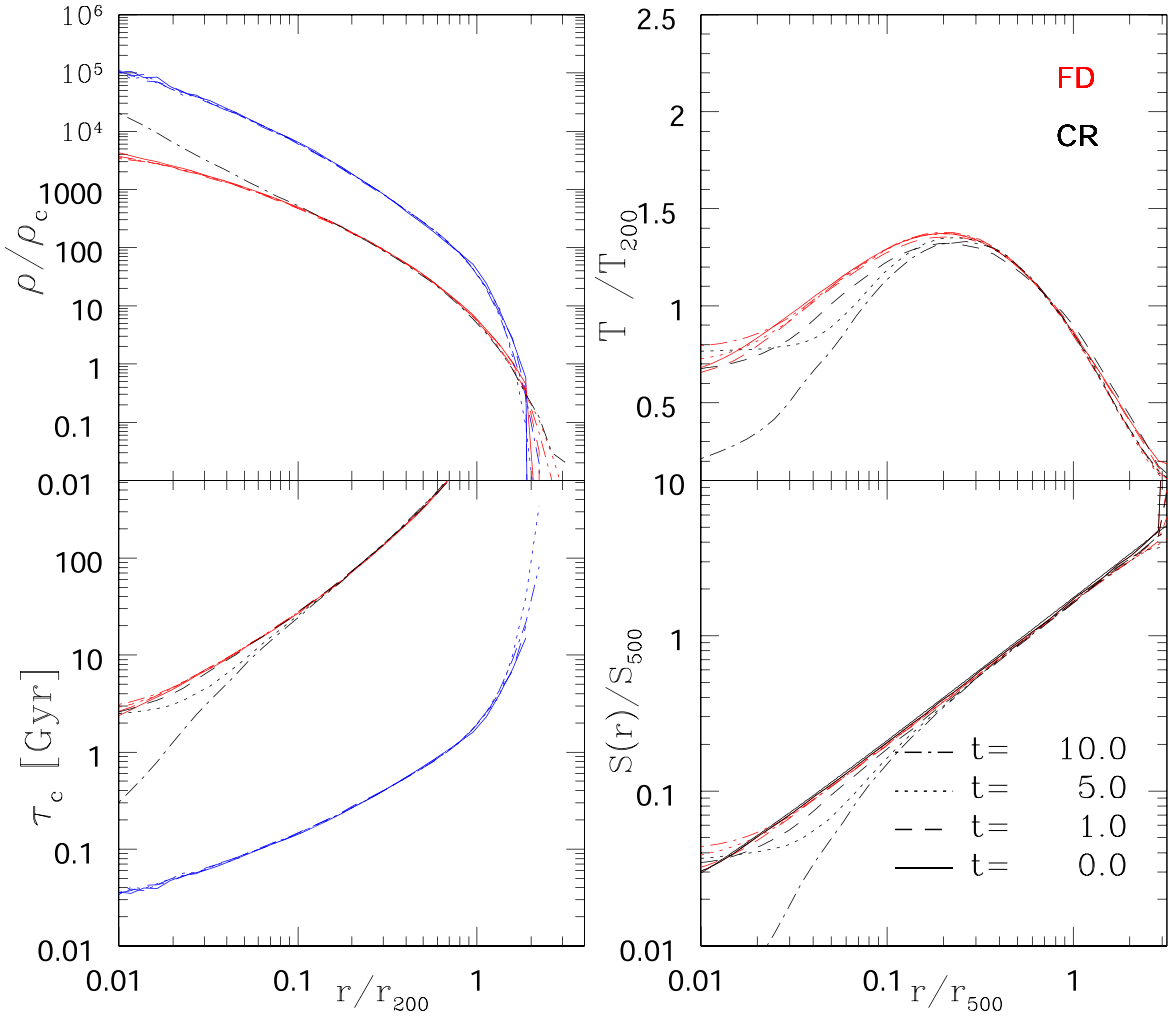

Figure 3. As in Fig. 2, time evolution for two isolated gas+DM haloes. The FD profiles refer to an halo initialized as the GL halo of Fig. 2, but with a friction term (30) added to the SPH momentum equation. The CR halo has the same initial conditions of the RD halo, but its gas evolution is followed by including radiative cooling in the SPH equations and without the presence of the damping term (30). For the sake of clarity, in the top left-hand panel the gas density profile of the CR halo is shown only for $t = 10$ Gyr.

It is instructive to compare the profiles of Fig. 4 with the corresponding ones shown by Z11 (figs 15 and 16 of his paper). There are strong similarities, but also interesting differences. In general, both density and temperature profiles have the same radial behaviour as the corresponding profile of Z11. In particular, for a specific mass ratio R, the hierarchy of the profiles at any given radius r is always reproduced. This is reassuring because it validates our setup procedure and the code we are using.

None the less, when contrasted against Z11 values, the central temperatures are found smaller by a factor lying in the range $\simeq 20 - 30$ per cent. Differences in the final profiles of thermodynamic quantities between our simulations and those of Z11 can be attributed to a number of reasons. To be specific, the largest impact will be caused by differences in the setup of the initial cluster kinematic and physical parameters, and by the different numerical hydrodynamical schemes used to perform the simulations. The latter can be significant, and in order to pin down its impact it is necessary to reduce as much as possible the effects of differing initial conditions.

To this end, we use as reference the merger with $R = 1{:}1$ and $b = 0$. This merging configuration has the advantage of having a very short collision time ($t_{\rm hit} \simeq 2$ Gyr), so that differences between our initial orbital settings and those of Z11 are minimized. In what follows, we will refer to this simulation in brief as $R1b0$.

For a better comparison of our merging simulations with those of Z11, we perform a head-on merging simulation with mass ratio $R = 1{:}1$ and initial conditions constructed as follows: The DM halo of each of the two clusters has a mass of $M_{200} = 6 \times 10^{14}\,{\rm M}_{\odot}$, equal to that of cluster C1 in Table 1, but we set the cluster radius to $r_{200} \simeq 1.55$ Mpc. This value is that reported in table 1 of Z11 for his cluster C1, and its a bit smaller ($\simeq 10$ per cent) than our corresponding value ($r_{200} \simeq 1.76$ Mpc).[2] Note that the concentration parameter is the same for the two clusters ($c = 4.5$). It must be stressed that this small difference in the cluster radii has a significant impact when comparing final results, such as entropy profiles. This is because small differences in the reference radius r_{500} or r_{200} (equation 24 or equation 1 of Z11) induce differences in the initial gas entropy at the same physical radius, which in turn imply much larger differences in the final entropy profiles.

[2]This difference is due to an error in the reported value of r_{200} (ZuHone, private communication).

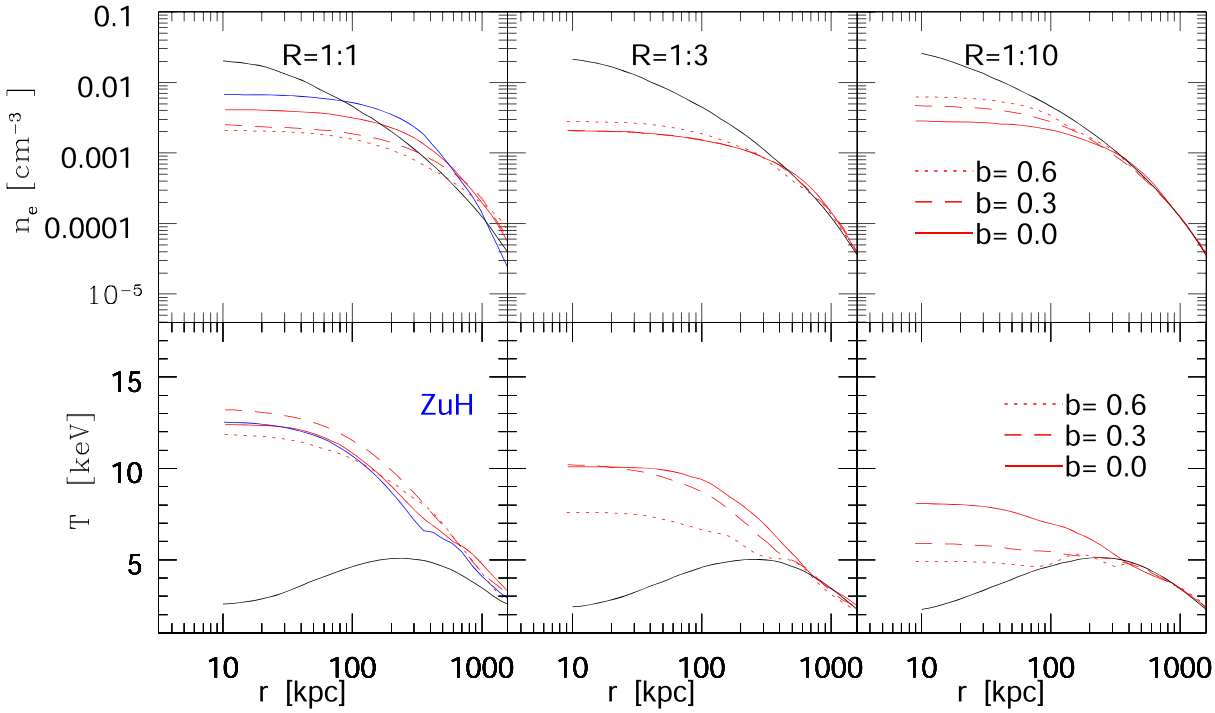

Figure 4. Final gas density (top panels) and mass-weighted temperature (bottom panels) profiles at $t = 10$ Gyr. From left to right, the mass ratios are $R = 1{:}1$, 1:3, and 1:10. Each bottom panel refers to the same cluster mass ratio R as the corresponding top panel. In each panel, the different line styles refer to merging runs with different impact parameters, while the solid black line shows the initial profile at $t = 0$ Gyr for the more massive subcluster. The origin is centred at the location of the gas density peak of the final merged system. The solid blue lines in the left-hand panels are the profiles extracted at $t = 10$ Gyr from a merging run with $R = 1{:}1$ and $b = 0$, but with the initial entropy profile being given as in Z11.

To construct our DM density profile, we truncate the cluster at a final radius $r_{\rm max} = \xi r_{200} = 1.4 r_{200}$, and adopt a decaying radius $r_{\rm decay} = 0.1 r_{200}$ (as in Z11). These radii are smaller than those adopted in our initial conditions: $(\xi,\ \eta) = (2,\ 0.2)$, but for this merging configuration the collision time is very short and the considerations of Section 2.2.1 about DM stability can be considered secondary. Moreover, as in Z11 we initialize our cluster centre of mass positions with a relative initial separation of $d_{\rm in} = (r^1_{200} + r^2_{200})$.

Finally, our initial gas profiles are constructed according to the procedures described in Section 2.2.2, but truncating the profiles at $r = r_{200}$ and using equation (1) of Z11 with the same parameters S_0 and S_1 to specify the initial entropy profile $S(r)$. In the following, we refer to this simulation as ZuH and we will use it as our reference run against which to contrast our simulation results with those of Z11. The initial physical settings and kinematics of the ZuH simulation are now identical to those of simulation S1 in Z11, so that differences between the final thermodynamic profiles of the two runs can be entirely attributed to the different numerical schemes used to perform the simulations.

In the left-hand panels of Fig. 4, the solid blue lines indicate the density and temperature profiles of this simulation extracted at $t = 10$ Gyr. The difference between these profiles and the corresponding ones of the $R1b0$ run (solid red lines) can then be interpreted as originating from the different settings in the initial conditions between the two simulations.

A visual inspection shows that the difference in the ZuH density profile and its Z11 counterpart S1 is minimal. Both of the profiles have the same central density ($n_e \simeq 10^{-2}\,{\rm cm}^{-3}$ at $r = 10$ kpc) and a knee at the same radius $r \simeq 300$ kpc. Similarly, the temperature profiles are also in accord. The left-hand bottom panel of Fig. 4 shows a central temperature of $\simeq$13 keV for the ZuH run, whereas in Z11 the central temperature of the S1 run is $T \simeq 14$ keV. These agreements strongly suggest the validity of the hydrodynamic code used here to carry out the simulations. We postpone further discussion of this topic to later when we address the radial behaviour of the final entropy profiles.

The final profiles of the $R1b0$ run can also be contrasted with the corresponding ZuH profiles in order to assess the impact of different initial conditions and collision parameters on the final merged cluster. In particular, Fig. 4 shows that the ZuH temperature profile is in good accord with the profile of its parent simulation, whilst it can be seen that in the inner cluster region ($r \lesssim 300$ kpc) the density profile $n_e(r)$ is higher than that of $R1b0$ by about a factor ~ 2 and has a steeper decline with radius at $r \gtrsim 500$ kpc.

This difference in the final density radial behaviour is a consequence of two distinct effects. In the ZuH simulation, the initial entropy profile is the same as that of Z11, and from fig. 15 (left-hand panel) of Z11 it is easily seen that this leads to a much steeper initial density profile than that of the $R1b0$ run. This initial difference is not destroyed during the merging phases and still has an impact on the density profiles at $t = 10$ Gyr. On the other hand, at large radii the initial ZuH density profile is truncated at $r_{\rm max} = r_{200}$, half the value of the $R1b0$ simulation. As already discussed in Section 2.2.2, this implies a significant leakage of gas particles in the cluster outer regions during the merger. Thus, the final gas density at large cluster radii will be smaller than in the $R1b0$ run.

These findings demonstrate that final differences between the gas cluster profiles of our simulations and those of Z11 can be entirely interpreted in terms of the adopted initial entropy profile. This will

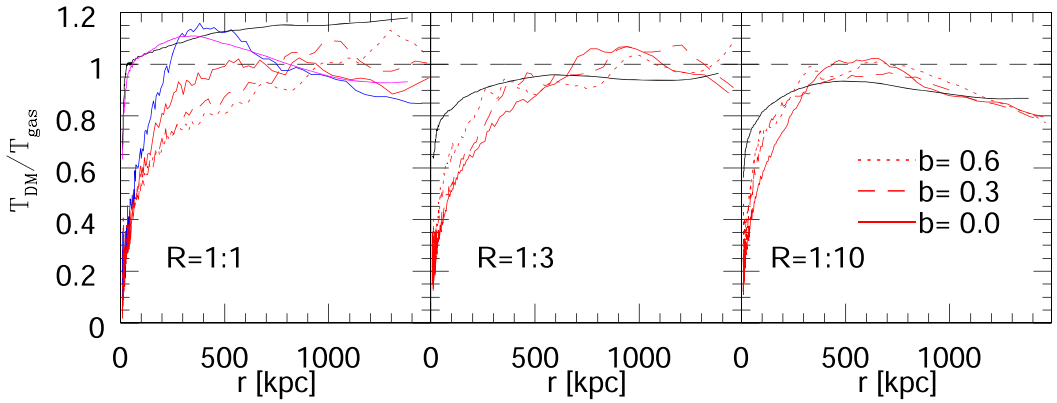

Figure 5. Final profiles of the DM-to-gas temperature ratio $T_{\rm DM}/T_{\rm gas}$. The meaning of the symbols is the same as in Fig. 4; the solid black lines show the initial profiles at $t = 0$ Gyr. In the left-hand panel, the solid magenta line refers to a merging run with $R = 1{:}1$ and $b = 0$, but having the DM haloes initially truncated at $r_{\rm max} = 1.4\, r_{200}$ instead of $r_{\rm max} = 2\, r_{200}$. The blue line shows the final profile of the ZuH run (see the text).

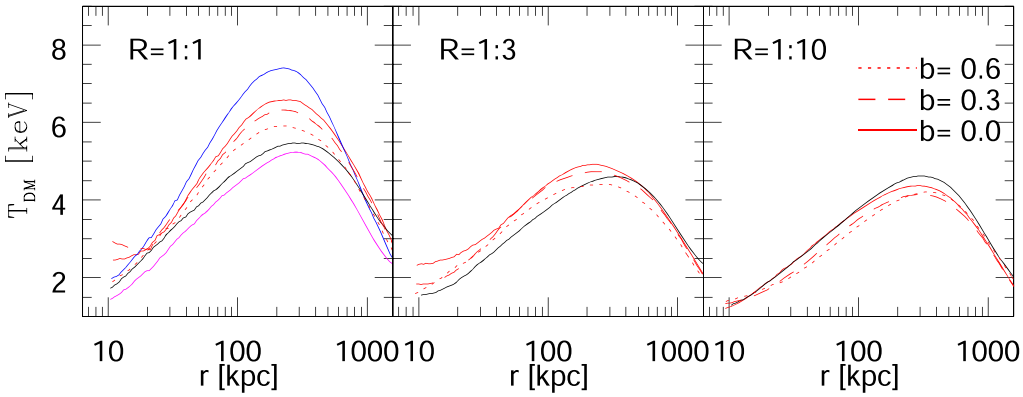

Figure 6. Final profiles at $t = 10$ Gyr of the DM temperature $k_B T_{\rm DM} = \mu m_p \sigma^2_{\rm DM}/3$. The panel presentation, colour coding, and line styles are the same as in Fig. 5. The solid magenta line in the left-hand panel is the initial DM temperature profile of the merging simulation with the smaller truncation radius.

be confirmed later when studying the radial behaviour of the entropy profile.

However, the approach used here to initialize cluster dark matter particle orbits differs in several ways from that of Z11. As can be seen in Figs 5 and 6, this has an impact on the final DM velocity dispersion $\sigma_{\rm DM}$ in several runs. For ease of comparison with the gas temperature $T_{\rm gas}$ and previous findings (Z11), we introduce the DM temperature $T_{\rm DM}$:

$$k_B T_{\rm DM} = \mu m_p \sigma^2_{\rm DM}/3. \tag{36}$$

Final profiles of the DM-to-gas temperature ratio $\kappa(r) \equiv T_{\rm DM}/T_{\rm gas}$ are shown at $t = 10$ Gyr in Fig. 5 for the different merging simulations. In accord with Z11 (fig. 19), the ratio $\kappa(r)$ is of the order of unity ($\simeq$0.9) at all cluster scales. The only exception is in the innermost cluster regions ($\lesssim$300 kpc) where the $\kappa(r)$'s tend to zero. This is expected, since baryons in the core will raise their entropy through mixing processes with post-shocked high-entropy material.

However, Fig. 5 shows that there is a significant difference between the initial ratio $\kappa(r)$ of the head-on merger with $R = 1{:}1$ and the others. In fact, for the $R1b0$ merger run the initial κ is systematically higher by $\simeq$20 per cent compared to the other simulations. This is in sharp contrast with the corresponding profile in fig. 19 of Z11, which does not exhibit such a feature and whose behaviour is in line with the others simulations.

We argue that this difference can be interpreted as originating from the adopted initial conditions. At variance with Z11, we initially set the centre of mass of our clusters separated by a distance $d_{12} = 2(r^1_{200} + r^2_{200}) \equiv d^{\rm in}$. The merging simulation time $t = 0$ is then defined when $d_{12} = d^{\rm in}/2$. This procedure then implies that at $t = 0$, the two clusters have already had time to interact. For the gas component, the impact on the initial profiles of this interaction is negligible (Fig. 4), but for the DM haloes one expects some amount of heating and an increase in the DM velocity dispersion. The strength of this effect will be weaker as the mass ratio R gets higher.

Fig. 6 shows the radial profiles $T_{\rm DM}(r)$, corresponding to the ratios depicted in Fig. 5. The left-hand panel ($R = 1{:}1$) shows that the initial profile $T_{\rm DM}(r)$ (solid black line) is a bit higher ($\simeq$ 20 per cent) than the initial profiles displayed in the other two panels ($R = 1{:}3$ and $R = 1{:}10$), thus confirming the previous reasoning. In fact, this effect is significant only when $R = 1{:}1$.

To demonstrate the correctness of this interpretation, we ran an additional merger simulations. As with the $R01b00$ run, we study a head-on merger with both cluster masses being $M_{200} = 6 \times 10^{14}\, {\rm M}_\odot$. At variance with the initial condition setup described in Section 2.2.1, here we truncate the DM haloes at a cut-off radius $r_{\rm max} = 1.4\, r_{200}$. We then perform the simulation and study the final $\kappa(r)$ and $T_{\rm DM}(r)$ profiles. If this heating effect depends on the cut-off radius $r_{\rm max}$, then at any given radius the final profiles of this simulation should approach the profiles of simulations with lower mass ratios. The profiles are shown (solid magenta lines) in Figs 5 and 6, and confirm these expectations.

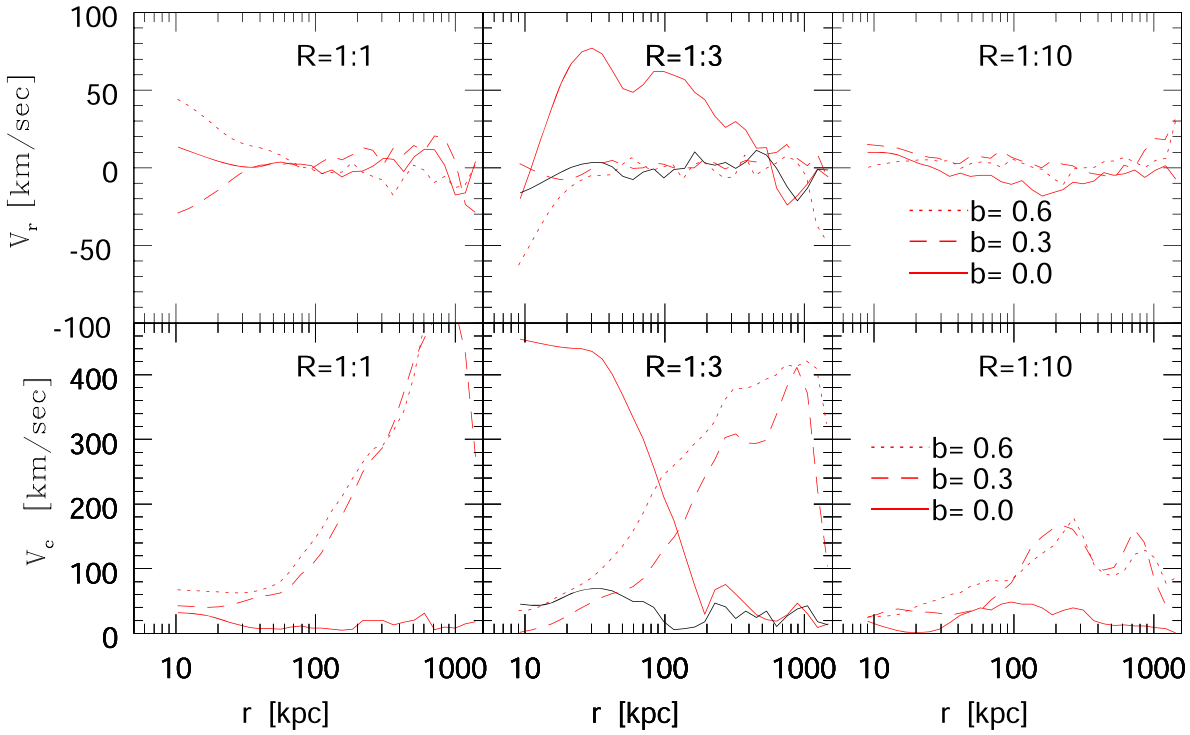

Figure 7. Mean gas radial (V_r, top panels) and circular (V_c, bottom panels) cluster velocities profiles at $t = 10$ Gyr for mergers without gas cooling. The meaning of the symbols is the same as in Fig. 4. The solid black lines in the middle panels refer to the profiles of the $R = 1{:}3$ and $b = 0$ run evaluated at $t = 11$ Gyr.

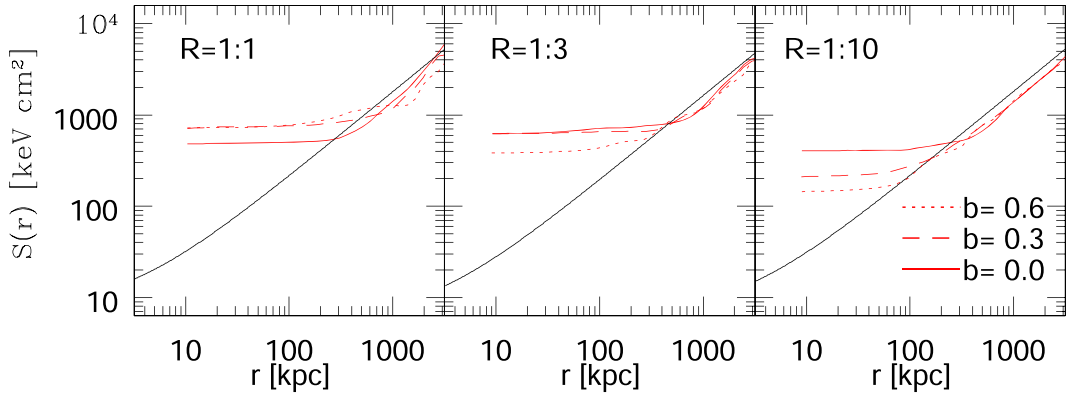

Figure 8. Final entropy profiles for the nine non-radiative merging runs at $t = 10$ Gyr (red lines). The panel presentation and line styles are identical to Fig. 4, solid black lines represent the initial entropy profile of the primary.

Finally, a comparison with fig. 18 of Z11 shows that the final profile $T_{\rm DM}(r)$ of the ZuH run (solid blue line, Fig. 6) is in accord with the corresponding profile of simulation S1. Moreover, at $r \simeq 200$ kpc the ZuH profile has a peak value ($\simeq$7.2 keV) that is about 15 per cent higher than the peak of the $R01b00$ run at the same location. This offset between the two runs in the peak of the final DM velocity dispersion is interpreted as originating from the differences in the adopted initial conditions. In particular, for simulation $R01b00$ the two clusters have initial radii of $r_{200} \simeq 1.76$ Mpc, whilst initially $r_{200} \simeq 1.55$ Mpc for the ZuH simulation.

We show in Fig. 7 the mean radial (V_r) and circular (V_c) gas velocities profiles at $t = 10$ Gyr. The latter is defined at the cluster radius r as $V_c(r) = \sqrt{\bar{v}_\phi^2(r) + \bar{v}_\theta^2(r)}$, where $\bar{v}_\phi$ and $\bar{v}_\theta$ are the mean azimuthal and polar velocities, respectively. The profiles of Fig. 7 can be contrasted with the corresponding profiles in figs 21 and 22 of Z11. All of them exhibit a radial behaviour which is in accord with their Z11 counterparts, with the only exception being the head-on $R = 1{:}3$ merger (simulation S4 of Z11). The final velocity profiles of this merged cluster are significantly different from those of simulation S4; in particular, the mean radial velocity is not close to zero. Values of $V_r \simeq 50\,{\rm km\,s^{-1}}$ persist up to $r \simeq 800$ kpc. Similarly, the circular velocity V_c is as high as $V_c \simeq 400\,{\rm km\,s^{-1}}$ within $r \lesssim 50$ kpc.

These values suggest that for this merger a fully relaxed status has not yet been achieved at $t = 10$ Gyr. To verify this possibility, we have continued the simulation until $t = 11$ Gyr. The velocity profiles corresponding to this epoch are shown in the middle panels of Fig. 7 as solid black lines, and they clearly show lower velocities.

Fig. 8 shows the final entropy profiles of the merged clusters. Note that the astrophysical entropy parameter $S \equiv kT/n_e^{2/3}$ is not the physical entropy and is not an extensive, additive quantity. Thus,

in averaging S over spherical shells, S was converted into the physical entropy (which is proportional to $\ln S$), and this was averaged over the spherical shell. Then, the average physical entropy was converted back to the entropy parameter S.

The presence of an entropy core is common to all of the profiles, with its level and extent depending on the mass ratio and impact parameter of the simulation. A comparison with the corresponding fig. 24 of Z11 shows a substantial agreement in the radial behaviour of the profiles, with differences in the central levels of core entropy which can be reconciled in light of the previous discussions.

In particular, at any specified radius and for a given mass ratio, the hierarchy of the entropy profiles as a function of the impact parameters is strictly reproduced. Following Z11, differences in the various levels of entropy profiles can be interpreted in terms of the different amounts of entropy mixing taking place during the mergers.

The core entropy of the primary increases during the merger owing to the mixing of low- with high-entropy gas. This high-entropy gas is made available by the secondary as it falls through the ICM of the primary and is ram pressure stripped. The gas of the secondary is then efficiently mixed with that of the primary through the development of Kelvin–Helmholtz instabilities. This scenario has been confirmed by various authors in several merging simulations (Takizawa 2005; Mitchell et al. 2009; ZuHone 2011).

Following this line of argument, the level of core heating of the primary should depend on the impact parameter b of the simulation. The higher the impact parameter, the lower is the amount of mixing. This follows because in off-centre collisions, the amount of gas stripped from the secondary depends on the ram pressure it encounters, and in turn on the initial mass ratio and angular momentum of the merger. For a given mass ratio the quantity of stripped material, which is available in the inner regions of the primary to raise core entropy through mixing, is then expected to depend sensitively on the orbit traced by the secondary.

In accord with this scenario, the third panel of Fig. 8 shows an increase in the central level of final entropy as the impact parameter decreases. However, this behaviour is clearly seen for the mergers with mass ratio 1:10 (third panel) but is progressively less pronounced as the mass ratio R becomes higher. In fact, for the 1:1 mass ratio case the dependence of the final core entropy level on the impact parameter b is reversed, i.e. the first panel of Fig. 8 shows that simulation $R01b06$ has an higher level of central entropy than $R01b00$.

The likely origin for this difference with the results from the $R = 1{:}10$ merger is that in the equal-mass mergers, a significant amount of core heating is provided dynamically by the secondary during the final merging with the primary. This effect is almost completely absent in the $R = 1{:}10$ cases, in which the mass of the secondary is small with respect that of the primary, and for off-axis mergers the secondary is totally stripped by instabilities before coalescing with the primary.

For a better understanding of this scenario, in Section 3.3 we present a thorough discussion of how entropy is generated during the merging process. For several merging runs, we investigate in detail the time evolution of entropy and other related quantities, in order to demonstrate how the final entropy profile of the merged clusters depends critically on the mass ratio and angular momentum of the collision.

3.2 Stability issues

As a convergence test, we compared the final entropy profiles for several merger runs with simulations in which we varied the numerical resolution and/or the adopted initial conditions.

For two equal-mass mergers ($b = 0$ and $b = 0.6$), in Fig. 9 (left-hand panel) we show the final entropy profiles together with those extracted from the corresponding higher resolution runs (HR, black lines). These simulations were performed by adopting the same initial conditions as the baseline runs, but with the particle masses reduced by a factor $\sim$4. The plots show a radial behaviour of HR profiles which is in excellent agreement with the corresponding standard resolution profiles, a result which leads us to conclude that the simulations presented here are numerically converged.

Similarly, the entropy profile (blue line) of the ZuH run is contrasted with its parent simulation S1 (open circles, the points are taken from fig. 24 of Z11). There is a significant agreement between the two profiles, the only exception being the outermost point ($r \simeq 1800$ kpc) for which the entropy of the ZuH simulation is higher than that of S1. This result is interpreted in light of the steepening of the ZuH density profile at large radii (Fig. 4). As already outlined, this outer behaviour follows from the adopted initial conditions and the lack of an external buffer surrounding the SPH particles.

This strict agreement between the entropy profiles of two independent simulations is very significant and it has a number of implications. First, for a given merging configuration, it definitively shows that the only parameter which determines the thermodynamic structure of the final merged cluster is the initial entropy profile. The other direct consequence is that the numerical scheme used here produces, for the same initial conditions, a final entropy profile which is identical to that obtained by Z11 using the adaptative mesh refinement (AMR) code FLASH. This is a non-trivial issue, and consistency between hydrodynamical test cases performed using Lagrangian SPH schemes and mesh-based codes has been the subject of many investigations.

Specifically, Agertz et al. (2007) found that the standard formulation of SPH (SSPH; Price 2012) fails to reproduce the results of several hydrodynamic test cases, when contrasted against those obtained from Eulerian mesh based codes. In particular, non-radiative SSPH simulation of galaxy clusters exhibit entropy profiles with a power-law behaviour. This is in sharp contrast with the constant entropy cores produced in Eulerian mesh simulations (Mitchell et al. 2009). These discrepancies are due, in part, to the intrinsic difficulty SSPH has in modelling density gradients around contact discontinuities, which in turn implies that there is a surface tension effect that inhibits the growth of fluid instabilities (Agertz et al. 2007).

To address these problems, several solutions have been proposed (Hopkins 2015, and references cited therein). In particular a possible solution is to add a dissipative term to the SPH thermal equation, with the purpose of smoothing the thermal energy at fluid interfaces (Price 2008; Wadsley et al. 2008). The presence of this AC term has the effect of smoothing entropy transitions at contact discontinuities, thus enforcing pressure continuity and in turn removing the artificial surface tension effect that suppresses the growth of the instabilities at fluid interfaces.

The SPH scheme employed here is based on this AC formulation, but the adopted signal velocity (equation 14) is different from that originally proposed by Price (2008) and it is better suited when gravity is present (Wadsley et al. 2008; Valdarnini 2012). Other formulations of SPH aimed at solving these issues are the SPH scheme proposed by Read & Hayfield (2012; SPHS), which is based on the use of a high-order dissipation switch, and the density-independent scheme of Saitoh & Makino (2016; DISPH). To validate these numerical schemes, it is important to assess the degree of consistency between the level and radial extent of the core entropies produced by these codes in cluster simulations. To this end, radial

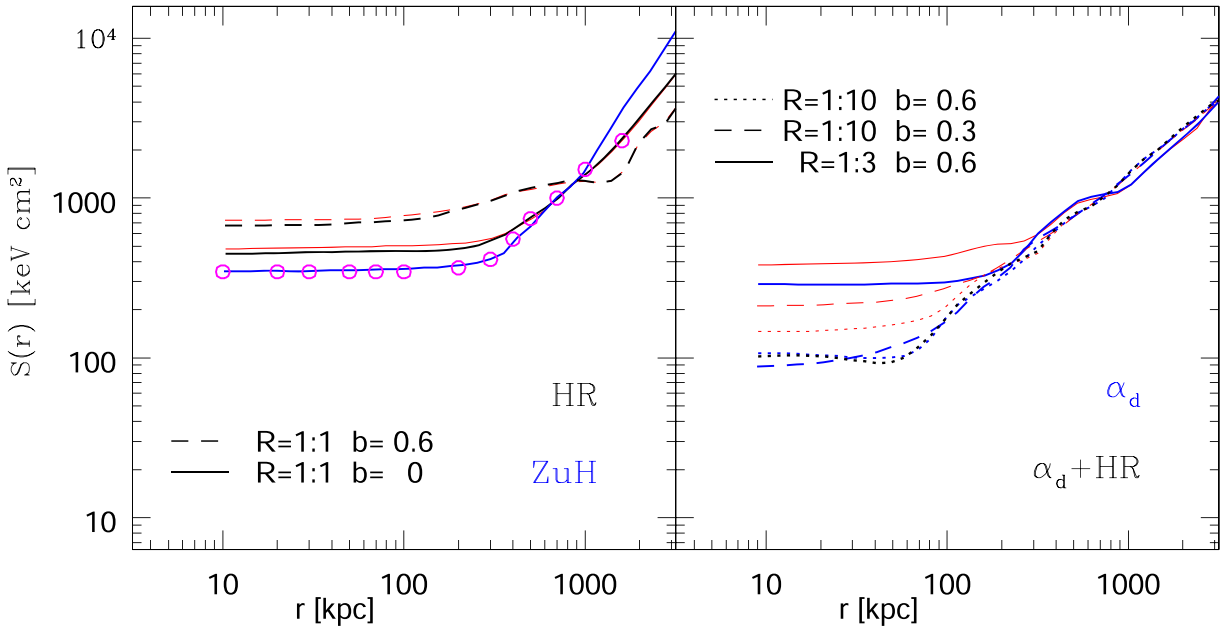

Figure 9. For several merging runs, final entropy profiles from Fig. 8 (red lines) are contrasted against the corresponding profiles extracted from merging simulations with different numerical parameters. Left-hand panel: black lines labelled HR show the entropy profiles of high-resolution simulations, performed by using a number of particles about four times higher than in the baseline runs. The solid blue line is the entropy profile extracted from a merging run with $R = 1{:}1$ and $b = 0$, but with its initial entropy profile identical to that in Z11. The open circles are taken from the entropy profile of the corresponding simulation S1, as given in fig. 24 of Z11. Right-hand panel: blue lines ($\alpha_{\rm damp}$) refer to merging runs in which the friction term is switched off at a simulation time $t > 0$ which depends on the impact parameter b. For the merging simulation $R = 1{:}10$ and $b = 0.6$, the black dots ($\alpha_d + HR$) are from a high-resolution run that also had the damping term switched off.

entropy profiles extracted from galaxy cluster simulations can be contrasted with the corresponding ones obtained from their AMR counterparts.

On this issue, the results reported in the literature show the absence of a general agreement between the various final entropy profiles. From DISPH simulations of galaxy clusters, Saitoh & Makino (2016) obtain final levels of core entropies which are intermediate between results from SSPH and those from AMR codes. Their entropy levels are also in accord with those obtained using the moving mesh scheme AREPO (Springel 2010), or the meshless code GIZMO (Hopkins 2015). These schemes are both based on Riemann solvers.

Sembolini et al. (2016) carried out a systematic comparison between the final entropy profiles extracted from a suite of simulations of an individual cluster. Their simulation set is constructed by using different codes. Their results showed that a flat inner entropy profile, such as that obtained using the AMR code RAMSES (Teyssier 2002), is similarly formed in cluster simulations produced using SPH variants which are based on some form of artificial dissipation. In particular, both the improved SPH code of Beck et al. (2016) and the SPHS scheme (Read & Hayfield 2012) give entropy profiles in accord with mesh-based results. The AC implementation of the former SPH scheme is very similar to the one employed here, thus reinforcing the consistency between our ZuH entropy profile and that of the corresponding S1 run of Z11.

It must be stressed that the core entropy level and size of the core are mainly regulated by the maximum value $\alpha^C_{\rm MAX}$ of the AC particle parameter α^C_i. For the simulations presented, here we set $\alpha^C_{\rm MAX} = 1.5$, this upper limit being derived from the consistency of self-gravity tests with mesh results (Valdarnini 2012). This limiting value is also in accord with the DISPH runs of Saitoh & Makino (2016), who concluded that a core entropy is established when $\alpha^C_{\rm MAX} \gtrsim 1$.

Power, Read & Hobbs (2014) criticized the AC formulation of SPH; based on the results from Wadsley et al. (2008), they suggest that the AC scheme may not always achieve numerical convergence. However, the HR profiles of Fig. 9 are fully converged and do not support this view. We argue that it is the adopted method to estimate gradients using a matrix inversion that is more relevant in this context. As demonstrated in V16, our scheme is seen to exhibit excellent convergence properties.

Finally, it must be emphasized that the strict agreement between the final entropy profile of our ZuH test run with the corresponding S1 profile of Z11 does not imply that the produced core entropy levels are correct. It just demonstrates that the two codes consistently obtain the same results, when adopting the same initial conditions. It remains unclear which is the correct core entropy level in these sort of simulations, with SSPH lacking of any mixing process and Eulerian codes having the tendency to overestimate mixing effects because of numerical diffusion (Springel 2010).

In the right-hand panel of Fig. 9, we analyse the consistency of our setup procedure for several merger configurations. Specifically, the friction parameter $\alpha_{\rm damp}$ introduced in Section 2.2.2 is switched off when the two cluster orbits have reached the initial conditions of Z11 ($t = 0$). This friction term is introduced to maintain a stable realization of the CC entropy profile before the occurrence of the cluster collision. However, in merging simulations with large angular momentum, the time interval between $t = 0$ and the direct collision can be large ($\gtrsim 5$ Gyr). For these mergers, a certain amount of numerical heating can modify the core of the original entropy profile before the collision (see Fig. 2), thereby increasing the final level of core entropy.

In order to assess the impact of this effect on the final entropy profiles, we ran three additional merger simulations. Among the

simulation suite, we have chosen three merging configurations with the criterion of having the highest angular momentum. These are the two merging simulations with mass ratio $R = 1{:}10$ and impact parameters $b = 0.6$ and $b = 0.3$, and the simulation with $R = 1{:}3$ and $b = 0.6$. For these simulations, the damping parameter $\alpha_{\rm damp}$ is switched off at a simulation time $t_{\rm hit} > 0$ and not at $t = 0$. This procedure guarantees that the initial entropy profile of the primary cluster maintains its form for a certain period of time after $t = 0$. Henceforth, we will generically refer to these simulations as α_d.

The choice of the time $t_{\rm hit}$ is a compromise between the need to avoid the possible numerical heating of the primary cluster core, and at the same time, to not damp significantly the primary core's heating due to entropy mixing driven by dynamical interactions with the secondary. As outlined in Section 2.3, we define $t_{\rm hit}$ approximately as the epoch when, after the first pericentre passage, the distance between the two clusters centre of mass becomes smaller than $\simeq r^{1}_{200}$.

Our estimates give $t_{\rm hit} \simeq 9$ Gyr for the merging simulation *R*10*b*06, and $t_{\rm hit} \simeq 5$ Gyr in the case of the *R*10*b*03 and *R*03*b*06 merging runs. Clearly, a higher value of $t_{\rm hit}$ leads to a longer time required for the damping term to keep the entropy profile stable.

The first value of $t_{\rm hit}$ corresponds to the maximum required period of damping, whereas in the case of off-axis mergers $t_{\rm hit} \simeq 5$ Gyr constitutes an approximate lower limit to $t_{\rm hit}$. This choice of different off-axis merger cases allows us to assess the impact of numerical heating on the entropy profile of the final merger remnant.

By comparing the final entropy profiles of these simulations (α_d, blue lines) in the right-hand panel of Fig. 9 with the corresponding ones in Fig. 8, we see that a certain amount of numerical heating is always present. All of the α_d profiles have core entropy levels systematically smaller than their standard counterpart. For instance, in the case of *R*03*b*06 the final central entropy of the α_d ran is smaller by about $\simeq 30$ per cent. For the other two merging simulations the difference is even higher, being almost a factor of two in the case of *R*10*b*03. Note that the core entropy levels of the α_d runs are now in better agreement with the corresponding ones displayed in fig. 24 of Z11.

Moreover, to demonstrate that the final profiles are numerically converged, for the simulation *R*10*b*06, we also run a high resolution simulation (α_d+HR, black dots). In Fig. 9, it can be seen that the entropy profiles of the two simulations are almost coincident, thus confirming that our simulations are not affected by insufficient resolution.

These results demonstrate that our setup procedures as described in Section 2.2 are not entirely free of relaxation effects, with some amount of numerical heating being present in the final entropy profiles of the merged clusters. The result of the α_d run with $R = 1{:}3$ and $b = 0.6$ suggests that this effect leads to an overestimate of the final core entropy level by $\simeq 30$ per cent. For the merging run *R*10*b*06 the increase is similar ($\simeq 50$ per cent), whereas for the merging simulation *R*10*b*03 the difference in the central entropy values is larger, $\sim$100 keV cm^2.

Thus, we conclude that with the setup procedure adopted here, in merger simulations with high angular momentum and a 1:10 mass ratio there is the tendency to overestimate final entropy in cluster cores by about $\simeq 30$ per cent. This relaxation effect can be compensated for by switching off the damping term at a later time $t_{\alpha_d} > 0$; however, the correct implementation of this correction requires a careful choice of t_{α_d} to avoid overcorrection leading to artificially lower entropy levels.

3.3 How is central entropy generated during mergers?

In this section, we examine the time evolution of entropy and other related quantities for several merger simulations. The analysis is aimed at investigating the origin and amount of final central entropy as a function of the initial merging parameters.

To this end, we construct radial profiles of gas density and entropy at given times. The radial profile of a given quantity is calculated for each radial bin by averaging grid values computed on spherical shells, defined by a set of $(\theta, \phi) = 40 \times 40$ grid points uniformly spaced in $\cos\theta$ and ϕ. Unlike in Section 3.1, the origin of the shells is centred at the gas density peak of the primary, tracked at run time. For equal-mass mergers we adopt the convention of defining as primary the cluster on the left in the $\{x, y\}$ plane of the collision.

We first discuss the head-on, 1:1 mass ratio case. This is the most energetic event and its dynamics are relatively simple. In the left-hand panel of Fig. 10, we show the time evolution of the gas density radial profile of the primary at different epochs. Similarly, the evolution of the entropy radial profile is shown in the right-hand panel. Additionally, we also show in the left-hand panel the density profile of the secondary; this quantity has been evaluated in the frame of the primary. The gas profiles of each cluster member are constructed separately by culling from the set of SPH particles the corresponding gas particles. These are tagged at the start of the simulation according to their membership.

We have chosen to evaluate the profiles at five different times: $t = 1.25$, 1.50, 1.54, 1.70, and 2 Gyr. These are centred around $t_p \sim 1.6$ Gyr, the epoch at which the distance between the centres-of-mass of the two colliding cores attains its first minimum. In other mergers with non-zero impact parameters, this epoch is identified as the first pericentre passage and we denote it as t_p.

From the time evolution of the profiles of Fig. 10, we conclude that most of the final core entropy is generated at the time t_p of the first core collision. From the right-hand panel, it can be seen that the level of central entropy is already at $S(0) \sim 300$ keV cm^2 at $t \simeq 2$ Gyr. This entropy level is about $\sim$70 per cent of its final value, as can be inferred from the right-hand panel of Fig. 8.

This scenario is also confirmed by the radial behaviour of the temperature profiles displayed in Fig. 11. The two panels show the temperature profiles of both primary and secondary at different times. As in Fig. 10, the secondary profiles are evaluated in the primary frame. To avoid overcrowding, we have divided the profiles in two categories: before (left-hand panels) and after (right-hand panels) the epoch $t_p = 1.6$ Gyr.

The left-hand panel of Fig. 11 shows how the temperature profile of the primary increases progressively, as the secondary approaches the primary and the gas is shock heated. This increase is first characterized by a peak in the primary outskirts, which moves inwards and gets wider at late times ($t \rightarrow t_p$). The temperature of the secondary increases too, in fact at $t = 1.54$ Gyr both the two core temperatures approach the same level. These findings consistently support the view that for head-on mergers most of the final core entropy is generated during the first core collision, with the remainder of the high-entropy gas being accreted later during the final phases of the merging.

A different scenario of entropy generation emerges when analysing mergers with an initial angular momentum (AM). We have chosen to discuss first the case of the off-axis merger with 1:1 mass ratio and $b = 0.6$. Among the equal mass mergers this has the highest AM, so its study is particularly interesting in order to analyse how entropy is generated during these collisions.

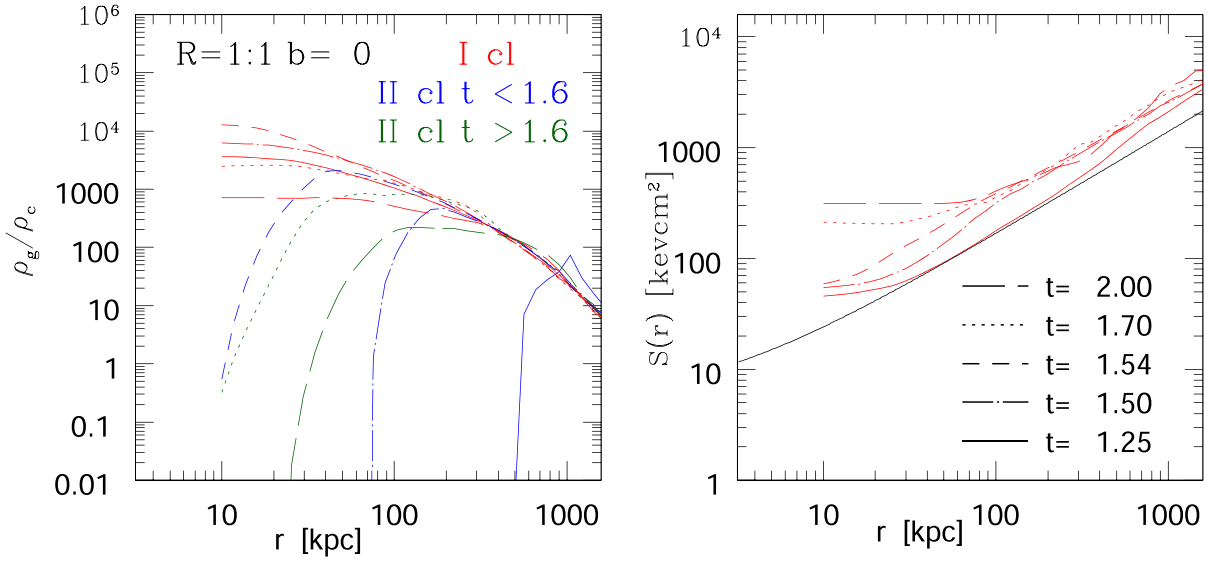

Figure 10. For the head-on 1:1 mass ratio case, we show radial profiles of gas density (entropy) in the left-hand (right-hand) panels. Different line styles refer to different epochs, and the time is in Gyr. In the left-hand panel, red lines indicate the gas density profiles of the primary (I), whilst blue and green lines those of the secondary (II). At each epoch the profiles of both clusters are evaluated in a frame centred on the peak of the gas density of the primary. For the secondary blue (green) lines are used to indicate profiles extracted at times before (after) $t \simeq 1.6$ Gyr, an epoch which is approximately identified as that when the distance between the two cluster centres-of-mass reaches its first minimum. Right-hand panels show the entropy profiles of the primary at different epochs. The solid black line refers to the initial profile.

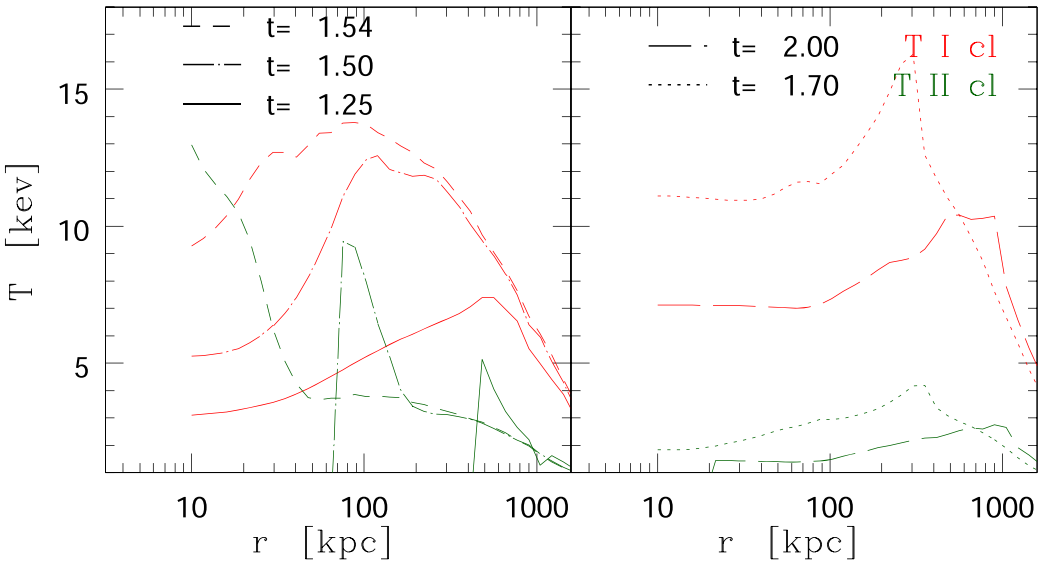

Figure 11. For the same merger as in Fig. 10, we show here the evolution of the gas temperature profiles, red lines are for the primary and green lines refer to the secondary. For the sake of clarity, in the left-hand panels we show profiles evaluated at $t < 1.6$ Gyr , when the two clusters are approaching each other, and in the right-hand panels, the profiles are evaluated at $t > 1.6$ Gyr, after the first pericentre passage. As in Fig. 10, at each epoch radial profiles are evaluated in the primary frame, with its origin being defined as the gas density peak of the primary tracked at run time.

The two panels of Fig. 12 depict density and entropy profiles as done in Fig. 10, but for the *R*01*b*06 merging run. In particular, the first pericentre passage occurs at $t_p \sim 2$ Gyr, and we show profiles extracted at five different times centred around this epoch.

From the entropy profiles displayed in the right-hand panel of Fig. 12 one can recognize that, unlike the head-on case, most of the core entropy of the primary is generated well after the pericentre passage, between $t \sim 3$ and $t \sim 5$ Gyr. This last epoch corresponds to when the secondary has passed the apocentre and is falling back on to the primary. Note that in the left-hand panel of Fig. 12, the density profile of the secondary at $t = 5$ Gyr extends closer to the core of the primary than at $t = 3$ Gyr.

At $t \gtrsim 3$ Gyr, core heating of the primary proceeds as previously discussed for the head-on merger, with the secondary coalescing with the primary and the low-entropy gas in the core being mixed with the high-entropy gas generated during the core collision. This suggests that we can decompose the generation of entropy in the central regions of the primary into two distinct phases: a first one when the primary has a grazing encounter with the secondary, and a second phase when the secondary finally collapses on to the primary.

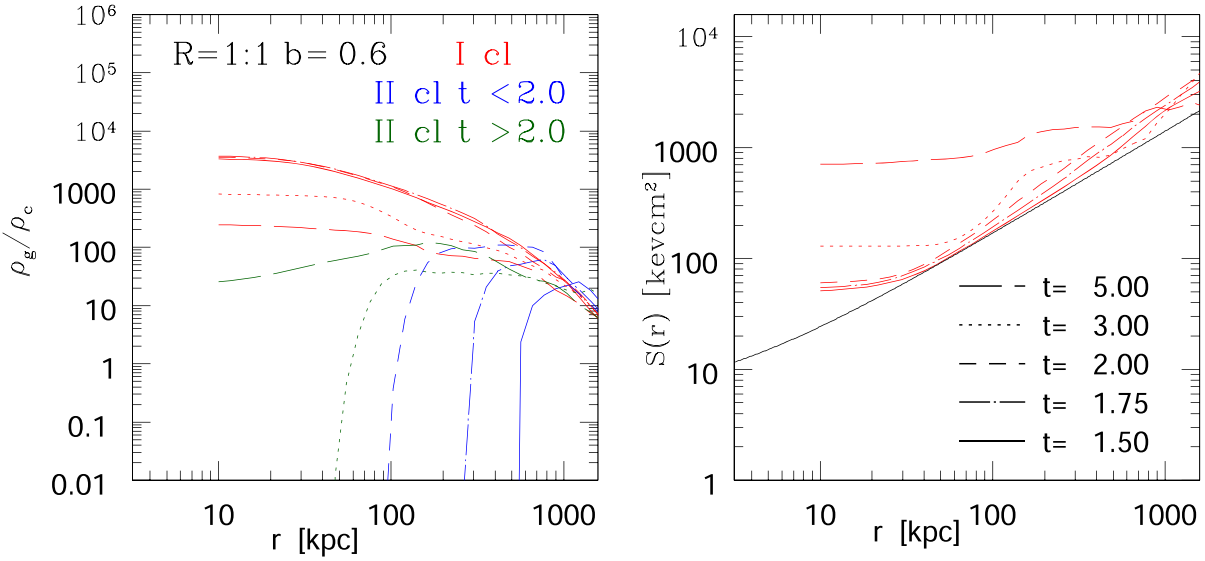

Figure 12. Identical to Fig. 10, but for the $R = 1{:}1$ off-centre merger with $b = 0.6$. The first pericentre passage occurs approximately at $t_p \simeq 2$ Gyr.

We now investigate how entropy generation proceeds during the first phase, when the secondary first approaches the primary.

To this end, we first show in the two panels of Fig. 13 the time evolution of the primary and secondary temperature profiles. Their time variations exhibit a behaviour in line with that seen with the corresponding profiles of Fig. 10, with a significant increase in the gas temperature of the primary at late epochs.

However, the right-hand panel of Fig. 12 shows a jump in the entropy of the primary between $t = 2$ and $t = 3$ Gyr. We argue that this entropy increase is a consequence of a transfer of AM between the secondary and the primary as the secondary is getting closer. This in turn is due to tidal torques that become significant as the two clusters reach their closest approach along their orbits.

This transfer of AM leads to an increase of the gas circular velocity of the primary and, subsequently, to the development of instabilities and entropy mixing. To better quantify this point, we show in Fig. 14 the radial profiles of the mean circular velocity $V_c(r)$ (left-hand panel) and artificial viscosity parameter $\alpha(r)$ (right-hand panel) for the primary cluster. The latter is constructed by radial averaging the AV parameters α_i in a manner similar to that adopted to calculate the other radial profiles. The mean velocity $V_c(r)$ is evaluated by subtracting the centre-of-mass velocity of the primary from the gas velocities. The profiles have been extracted at the following epochs: $t = 2$, $t = 2.5$, $t = 2.75$, $t = 3$, and $t = 5$ Gyr.

The time evolution of the mean circular velocity profiles reveals several important features. In particular, there is a progressive increase in the amplitude of the profiles as $t \to 3$ Gyr. All of the profiles at different epochs have the tendency to reach their peak values around ∼100–200 kpc, these are of the order of ∼600 km s^{-1} at $t \gtrsim 3$ Gyr.

This behaviour is shared by the corresponding artificial viscosity profiles $\alpha(r)$, which at epochs $t \gtrsim 3$ Gyr exhibit peak values of ∼0.12–0.15 in the same radial range. This clearly shows evidence of significant gradients in the flow velocity at ∼100–300 kpc, induced by the strong increase in the gas rotational motions.

These motions will generate local instabilities in the medium which in turn will lead to the development of turbulence, thus driving the diffusion of entropy. This is indirectly confirmed by the radial behaviour of the AC profiles $\alpha^C(r)$, which are constructed from the AC parameters α_i^C in the same way as we did for the AV profiles $\alpha(r)$. The qualitative behaviour of the profiles $\alpha^C(r)$ mirrors very closely that of the corresponding $\alpha(r)$, thus showing the presence of diffusive processes associated with the appearance of rotational motions.

We argue that the increase in core entropy seen between $t = 2$ and $t = 3$ Gyr is then a consequence of the rotational gas motions, induced by the passage of the secondary at the pericentre. However, to validate this picture, the local diffusion time-scale must be of the same order or lower than the estimated time-span (∼1 Gyr) over which entropy undergoes its changes. To further elucidate this issue, we now try to assess the diffusion time-scale associated with the development of Kelvin–Helmholtz instabilities (KHI).

The generation of KHI leads to the development of turbulent motions and to the formation of eddies at different spatial scales. The size of these eddies is expected to be significant, with scales of $\lambda \sim$ 100–300 kpc (Takizawa 2005; Subramanian, Shukurov & Haugen 2006). These estimates are also in accord with length scales found in simulations aimed at studying turbulent properties of the ICM (Vazza, Roediger & Brüggen 2012; Valdarnini 2019, see in particular fig. 9 of the first authors).

From equation (8) of Vazza et al. (2012), we estimate the coefficient for turbulent diffusion as given by

$$D_{\rm turb} \simeq 0.1\lambda\sigma \simeq 3\times 10^{30}\left(\frac{\lambda}{100\,{\rm kpc}}\right)\left(\frac{\sigma}{1000\,{\rm km\,s^{-1}}}\right)\,{\rm cm^2\,s^{-1}}, \tag{37}$$

and the corresponding diffusion time-scale by

$$\tau_D \simeq R^2/D_{\rm turb} \sim 3\left(\frac{R}{100\,{\rm kpc}}\right)^2\frac{1}{D_{30}}\,{\rm Gyr}\,, \tag{38}$$

where σ is the gas velocity dispersion, $D_{30} \equiv D/(10^{30}\,{\rm cm^2\,s})$, and R is the considered scale.

Between $t = 2$ Gyr and $t = 3$ Gyr the gas velocity dispersion of the primary is found to change drastically from ∼800 km s^{-1} down to ∼200 km s^{-1} within radii $r \leq 100$ kpc. By assuming an upper limit of $\lambda \sim 300$ kpc for KHI eddies, in the given time interval we then obtain values of D_{30} lying in the range $7 \lesssim D_{30} \lesssim 1.8$. This correspondingly gives $0.4 \lesssim \tau_D/(R/100\,{\rm kpc})^2\,{\rm Gyr} \lesssim 1$ between

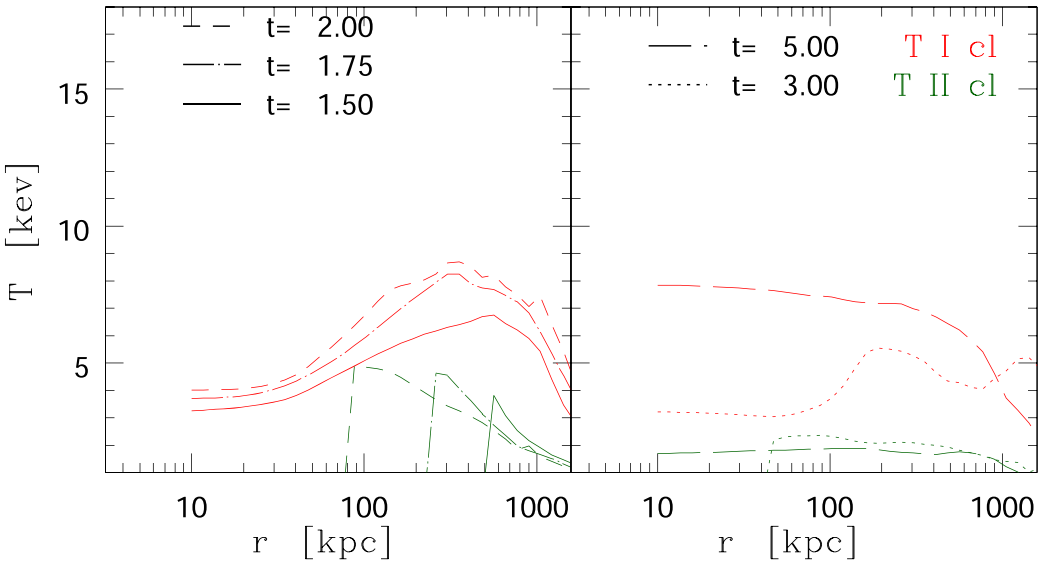

Figure 13. As in Fig. 11, for the merging case of Fig. 12 ($R = 1{:}1$, $b = 0.6$), we show here the time evolution of the gas temperature profiles for both the primary and secondary cluster.

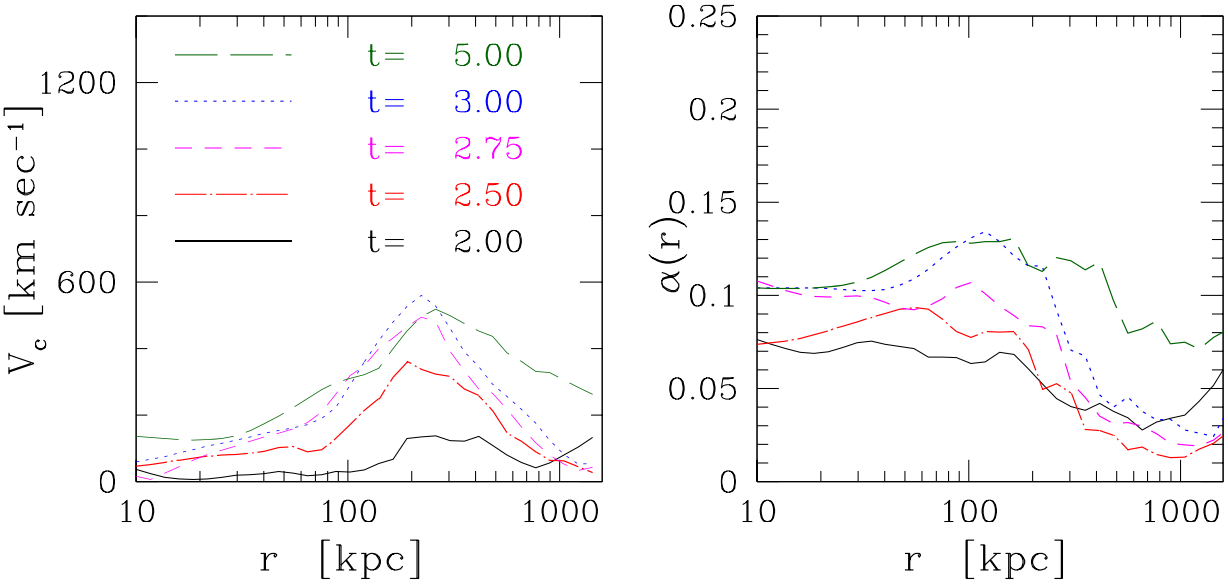

Figure 14. Average radial profiles of the mean circular velocity $V_c(r)$ (left-hand panel) and artificial viscosity parameter $\alpha(r)$ (right-hand panel) are shown at different epochs for the primary cluster of the merging run of Fig. 12. The centre-of-mass velocity of the primary has been subtracted from the mean gas velocities before evaluating the velocity profiles. The $\alpha(r)$ profiles have been extracted from the AV parameters α_i of the gas particles of the primary cluster, in the same way in which the radial profiles of other gas properties (e.g. temperature) have been derived. Time is in Gyr.

$t = 2$ Gyr and $t = 3$ Gyr, showing the consistency of the diffusion time-scale with the increase in central entropy seen between $t = 2$ and $t = 3$ Gyr at $r \leq 100$ kpc.

To further elucidate this critical point, we show in Fig. 15 the entropy profiles of the primary at different epochs. Unlike in the right-hand panel of Fig. 12, we show the radial entropy profiles extracted from a wider range of time frames; moreover, for each radial bin we also evaluate the entropy dispersion $\sigma_S(r)$. As noted in the text discussing Fig. 8 above, the average S over a spherical shell is determined by converting the entropy parameter S into a physical entropy, averaging this, and then converting the mean physical entropy back to $S(r)$. Similarly, the dispersion of the physical entropy is added and subtracted from the mean physical entropy, and these two values are converted back to S to give the upper and lower limits of the error bars in Fig. 15.

Within each panel of Fig. 15, we show the entropy profiles at two distinct epochs; for the sake of better understanding the profile referring to the latest epoch is shifted upwards by one order of magnitude. The time evolution of these entropy profiles clearly illustrates a progressive increase in entropy at outer radii, with a subsequent propagation towards the inner regions. If we now adopt the reasonable assumption that the entropy dispersion $\sigma_S(r)$ can be taken as a metric for assessing the amount of mixing present at that radius, $\sigma_S(r)$ (and presumably mixing) are initially very small at radii $r \lesssim 500$ kpc. The entropy dispersion becomes progressively wider in the outer regions of the primary as the secondary approaches

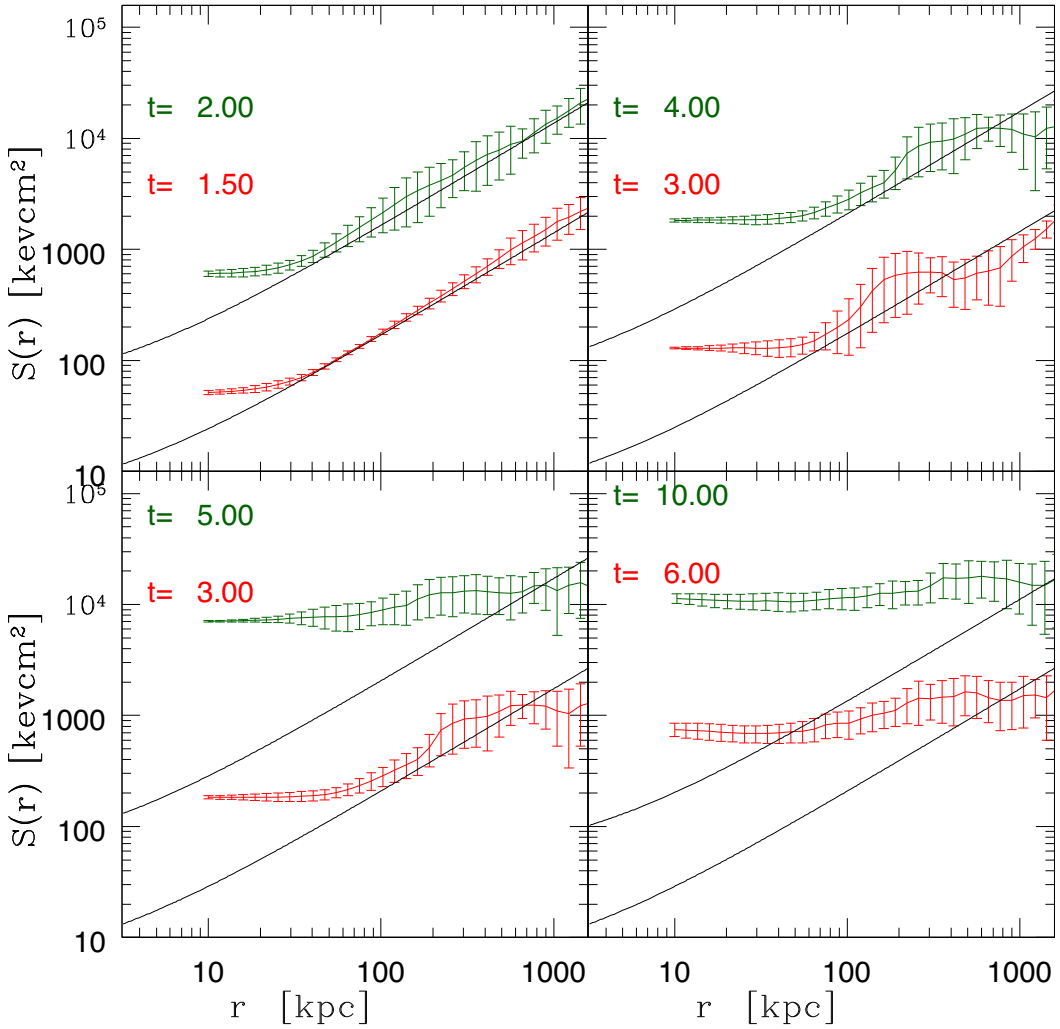

Figure 15. For the equal-mass merger with $b = 0.6$ of Fig. 12, we show here the entropy profiles of the primary at different epochs. At a given time, we compute the entropy dispersion (the error bars) by averaging over angular grid values of the shell for each radial bin (see the text). As in Fig. 12 the solid black lines refer to the initial profile. For the sake of clarity, in each panel the entropy profile referring to the later epoch has been shifted upwards by a factor 10.

($t \rightarrow t_p \approx 2$ Gyr), but with an amplitude which is still negligible within $r \lesssim 100$ kpc at $t = 2$ Gyr. At $t = 3$ Gyr, there is a widening of $\sigma_S(r)$, which is significant at radii $r \gtrsim 100$ kpc. However, it is only when $t \gtrsim 5$ Gyr that the entropy dispersion is approximately constant across all the cluster and the gas has now a higher degree of mixing. To summarize, we conclude that for the considered merging configuration, part of the final core entropy owes its origin to rotational motions induced by tidal torques occurring during the collision.

We now discuss the two off-axis mergers for the 1:10 mass ratio case. Fig. 16 is the analogue of Fig. 10 but for the $R = 1{:}10$ and $b = 0.3$ ($t_p \sim 1.6$ Gyr) merging, and Fig. 17 for $b = 0.6$ ($t_p \sim 2$ Gyr). In both cases the level of central entropy at late times is around $\sim$100 keV cm^2, while in the left-hand panel of the figures the time evolution of the secondary density profiles shows a negligible interaction with the primary's core. In fact, for the $b = 0.6$ merging the impact of the secondary on the density profile of the primary at $t = 4$ Gyr can be considered completely absent.

As already discussed in Section 3.2, in merging simulations with 1:10 mass ratio and AM, numerical heating effects can modify the level of core entropy before the two clusters merge together. For instance, one can assume that for the $b = 0.6$ run, all of the core entropy increase at $t = 4$ Gyr is due to this effect. This level can be contrasted with that expected in an isolated halo when the damping term is absent. From the GL run in the right-hand panel of Fig. 2, we obtain an entropy value of $S/S_{500} \simeq 0.15$ at $r/r_{500} = 0.1$ at $t = 5$ Gyr. This translates into $S \sim 130$ at $\sim$115 kpc, where we have taken S_{500} and r_{500} from Table 1. This implies that at the same epoch, for the $b = 0.3$ merging, at most $\sim$30 per cent of the entropy core level is due to merging effects.

To illustrate the impact of this effect, in Fig. 18 we depict density and entropy profiles for the $R = 1{:}10$ and $b = 0.3$ merger at various epochs, but extracted from the corresponding α_d simulation presented in Section 3.2. For this simulation, the damping parameter $\alpha_{\rm damp}$ was switched off at a simulation time $t_{\rm hit} = 5$ Gyr in order to stably maintain the initial entropy profile until $t = t_{\rm hit}$. The density profiles are time-centred around $t = 7$ Gyr, an epoch at which the secondary begins to coalesce with the primary.

The final entropy profiles depicted in the right-hand panel of Fig. 18 show a core entropy level of $\sim$100 keV cm^2 at $t = 10$ Gyr. This level is in accord with previous findings and demonstrates that in mergers with low mass ratios and AM, the bulk of core

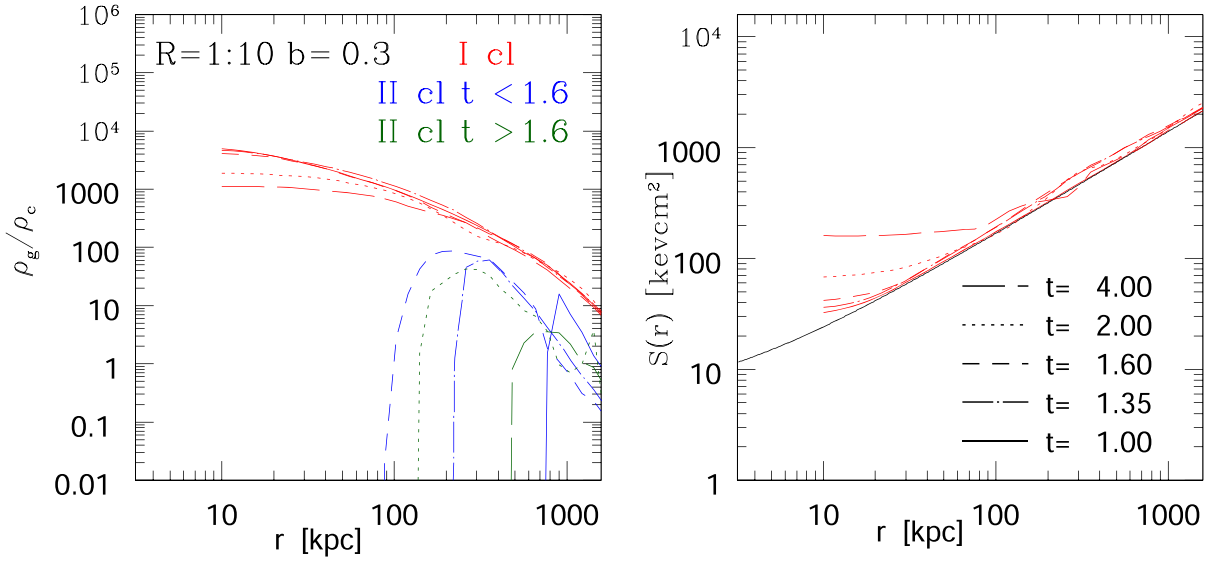

Figure 16. The same as Fig. 10, but for the $R = 1{:}10$ off-centre merger with $b = 0.3$. The first pericentre passage is estimated to occur at $t_p \simeq 1.6$ Gyr.

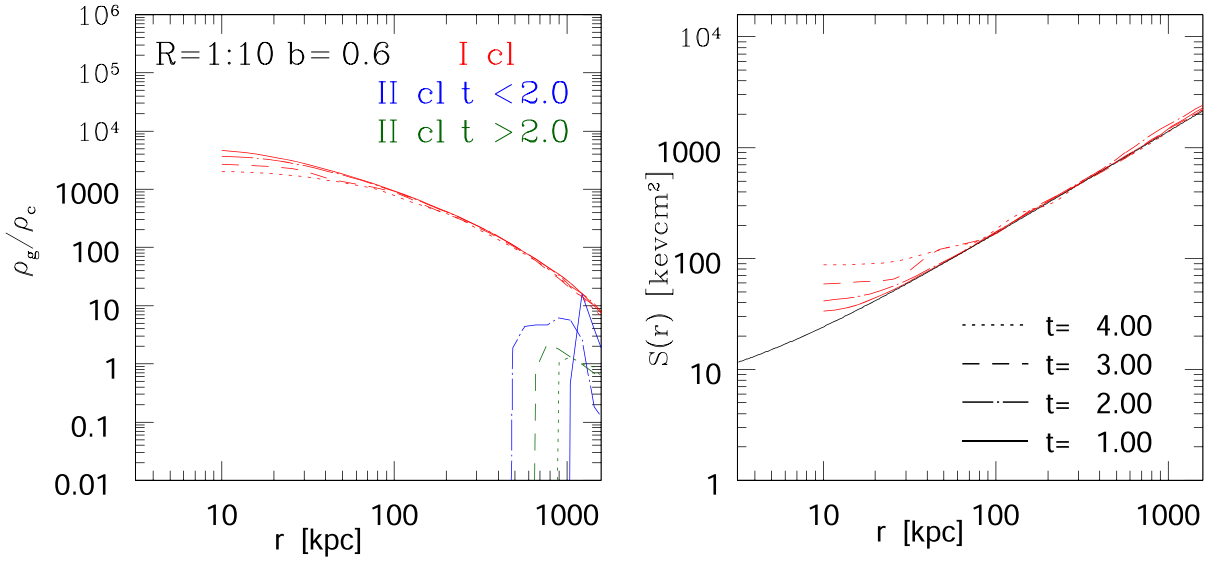

Figure 17. The same as in Fig. 16, but for the off-centre case with $b = 0.6$. Here the first pericentre passage is around $t_p \simeq 2$ Gyr.

heating occurs at late stages. A similar level of core entropy at $t = 10$ Gyr is obtained from the α_d simulation with $b = 0.6$ (Fig. 9).

To summarize, our findings indicate that heating of the core in off-axis mergers depends critically on the initial merging mass ratio as well as on the AM of the system. For equal-mass mergers and high AM, a significant contribution to the central entropy level is sourced by instabilities generated by tidal torques, as the secondary first reaches its pericentre. On the contrary, for unequal-mass mergers with 1:10 mass ratio, the secondary is progressively disrupted along its orbit by ram pressure and the development of hydrodynamical instabilities, and core heating becomes significant only during the late merging phases.

3.4 Radiative runs

We now investigate the heating of gas cores and the survival of CCs in a more realistic set of merging simulations. In this section, we present results extracted from simulations where the physics of the gas includes cooling, star formation, and energy feedback following supernova explosions.

The computational cost of these simulations is much higher than that of their adiabatic counterparts. Because of cooling, the development of short cooling times and large central densities during the simulations requires very small time-steps. For this reason, we refrain from resimulating all of the merging cases previously discussed and perform radiative simulations only for several of them. Additionally, we also present results from a merging run with a new initial condition set-up (see later).

As described in Section 3.2, merging simulations with cooling are initialized as in the adiabatic case. The cooling term Q_R in equation (12) is switched on at times $t > 0$, so that both adiabatic and radiative simulations start at $t = 0$ with the same profiles. For the chosen cases we show in Fig. 19 the final entropy profiles of the radiative merging simulations. These are contrasted with the profiles of the corresponding adiabatic runs.

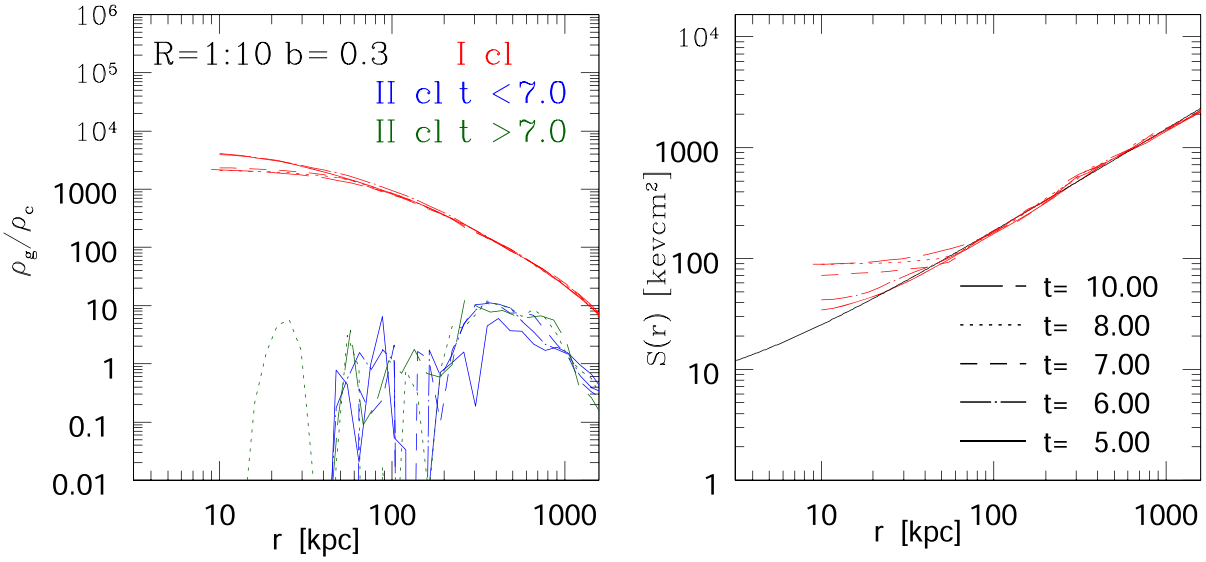

Figure 18. The same as for the merging case shown in Fig. 16, but for the α_d simulation of Section 3.2 (see the text), in which the parameter $\alpha_{\rm damp}$ is switched off at a simulation time $t_{\rm hit} = 5$ Gyr. The first pericentre passage is between $t = 1$ and $t = 2$ Gyr, and after it the secondary falls back on to the primary shortly after $t = 7$ Gyr.

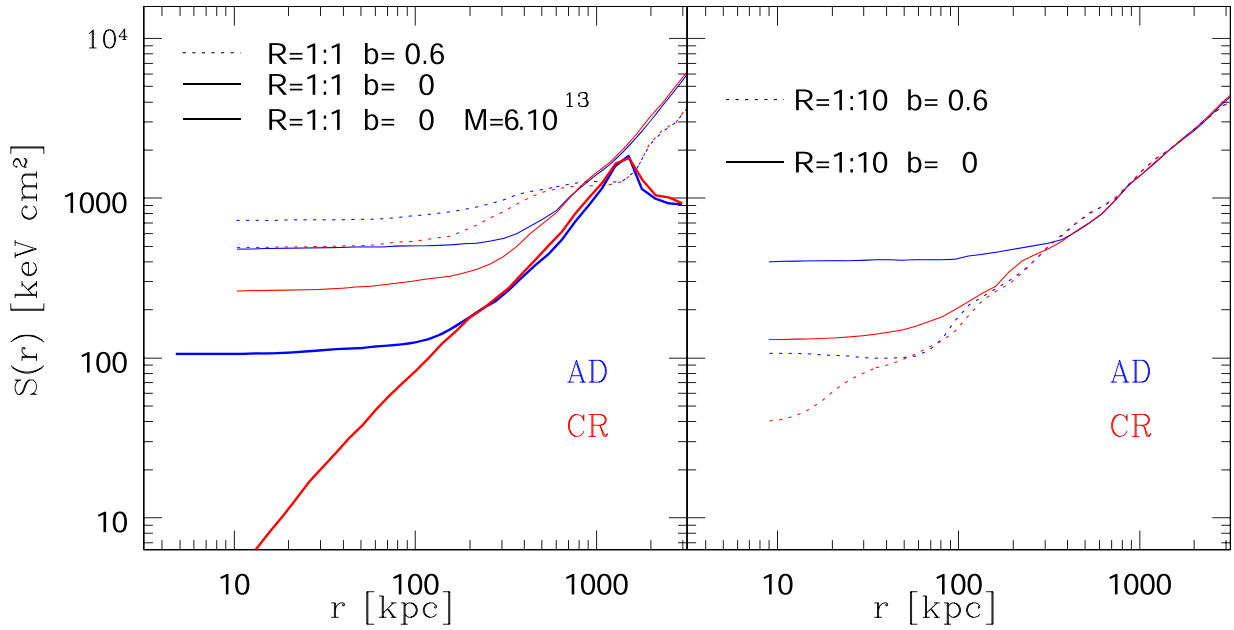

Figure 19. Final entropy profiles extracted from adiabatic (AD: blue lines) and cooling simulations (CR: red lines). The left-hand panel shows some runs with the mass ratio $R = 1{:}1$ and the right-hand panels refers to merging simulations with mass ratio $R = 1{:}10$. In the left-hand panel, thick lines indicate an head-on merging with cluster masses $M_1 = M_2 = 6 \times 10^{13}\,{\rm M}_\odot$.

In these simulations, the final level of core entropy, and as a consequence the CC ability to maintain its integrity, will depend on the various processes which have contributed to the core heating during the merging. We thus expect shock heating and entropy mixing to be counteracted in part by radiative cooling in shaping the central entropy profile of the merged remnant.

A discriminant criterion to assess whether or not the CC is destroyed during the merger is the level to which the central entropy is raised during the collision because of the heating processes. If this amount of entropy is high enough to raise the central cooling time, let's say above several Gyrs, then the CC cannot be re-established in a Hubble time. This implies the survival of CCs to be strictly related to the energetics of the collisions, i.e. to the mass ratio and initial orbit of the merger.

While the inclusion of gas cooling in the simulations will lead to the development of large gas core densities, the growth of KHI and the degree of gas mixing are not expected to be modified in a significant way when compared to the adiabatic runs. Damping of KHI in the presence of cooling will occur whenever $\tau_c < \tau_s$ (Vietri, Ferrara & Miniati 1997), where τ_s is the sound crossing time of the

perturbation. We estimate τ_s as λ/c_s:

$$\tau_s \simeq 0.2 \frac{\lambda}{100\,\mathrm{kpc}} \frac{1}{\sqrt{kT/\mathrm{keV}}}\,\mathrm{Gyr}\,. \quad (39)$$

From the previous discussion in Section 3.3, we adopt a lower limit of $\lambda \gtrsim 100$ kpc for the eddy size. The lower value of τ_c is about $\sim$1 Gyr in the core (Fig. 3), and it reaches $\sim$10 Gyr at $r \sim 100$ kpc. From the profiles of Figs 11 and 13, we estimate gas temperatures in the range of few keV in the cluster central regions. Therefore, we conclude that the impact of cooling on the growth of KHI can be considered negligible, in line with previous findings (ZuHone, Markevitch & Johnson 2010).

The final entropy profiles (red lines) of several equal-mass radiative merger simulations are displayed in the left-hand panel of Fig. 19. We first consider the two merging cases with impact parameter $b = 0$ and $b = 0.6$, previously investigated in Section 3.3. For the sake of comparison their adiabatic counterparts are also shown (blue lines).

In the head-on case we expect the core entropy to undergo a very steep increase because of the strong shock following the collision of the cores, with a subsequent decrease due to radiative cooling. The difference at $t = 10$ Gyr between the core entropy of the adiabatic simulation and the radiative one (solid lines, left-hand panel of Fig. 19) is $\Delta S(0) \simeq 200\,\mathrm{keV\,cm^2}$.

The off-axis merger (dot lines) exhibits a similar difference in final core entropies. In Fig. 20 we show the time evolution of density and entropy profiles for this run, as we did in Fig. 12 for the adiabatic case. A comparison between the two sets of entropy profiles shows a much more modest increase in entropy for the cooling run.

In fact, at $t = 5$ Gyr the level of core entropy is about $S_{cr}(0) \simeq 100\,\mathrm{keV\,cm^2}$, while in the adiabatic run it is about $S_{\mathrm{ad}}(0) \simeq 800$ keV cm^2. The difference is subsequently reduced soon after $t = 5$ Gyr, as the secondary finally merges with the primary and the process raises the central entropy up to $S_{\mathrm{cr}}(0) \simeq 500\,\mathrm{keV\,cm^2}$ at $t = 10$ Gyr.

This is in accord with Poole et al. (2008). From their merging simulations the authors argue that to re-establish a CC it is necessary for the remnant to be relaxed for a significant fraction of the cooling time τ_c. For the considered merger, we estimate $n_e(0) \sim 10^{-2}\,\mathrm{cm^{-3}}$ at $t = 5$ Gyr and $\tau_c(0) \sim 6\left(S(0)/100\,\mathrm{keV\,cm^2}\right)^{1/2}$ Gyr $\simeq 6$ Gyr, from equation (35). This time-scale is larger than that set by the final collision of the secondary, which raises again the central entropy and in turn τ_c to above $\sim$10 Gyr.

Finally, note that in the left-hand panel of Fig. 20 the density profile of the secondary is significantly reduced in the cluster inner regions, when contrasted with the adiabatic case at $t = 5$ Gyr. Similarly, in the same regions the core gas density of the primary is higher by a factor $\sim$5. These differences follow because of radiative cooling, with the primary developing a steeper profile than the secondary.

In the right-hand panel of Fig. 19, we show the entropy profiles of two unequal mass mergers with the mass ratio $R = 1{:}10$. The dynamics of the head-on case mirrors that of the $R = 1{:}1$ merging, but to a lesser extent because of the reduced mass of the secondary. There is a smaller increase in entropy as the two core collide, with radiative losses subsequently reducing entropy down to $S_{\mathrm{cr}}(0) \simeq 100\,\mathrm{keV\,cm^2}$ at $t = 10$ Gyr. In contrast to the adiabatic case, this level of core entropy is a factor ~ 2 smaller.

In the most off-centre ($b = 0.6$) merger, the impact of the secondary on the core is negligible. As in the adiabatic case, low-mass subclumps with large AM are progressively disrupted by instabilities before being able to significantly shock-heat the primary's core. However, in the adiabatic run there is a certain amount ($\Delta S(0) \simeq 100\,\mathrm{keV\,cm^2}$) of core heating taking place during the late phases ($t \sim 9$–10 Gyr) of the merger. This small entropy jump is now absent because of radiative losses, thus allowing the CC to survive.

Additionally, we ran another head-on radiative merging simulation with the mass ratio 1:1. In contrast to the merging case previously discussed, for the two clusters we now adopt a halo mass of $M_{200} = 6 \times 10^{13}\,\mathrm{M_\odot}$. The initial condition set-up being the same as described in Section 2.2.

For this simulation, we show in the right-hand panel of Fig. 19 the final entropy profile of the merger remnant (solid thick line), together with the profile of its adiabatic counterpart. The entropy profile of the radiative run exhibits a near power-law behaviour and, unlike the head-on $R = 1{:}10$ merging case, the CC has been rapidly re-established. This happens because now the mass of the primary is an order of magnitude smaller, thus the collision with the secondary (at $t \sim 2$ Gyr) is able to raise the central entropy only up to $S(0) \simeq 80\,\mathrm{keV\,cm^2}$. This is a factor ~ 2 smaller than in the the head-on $R = 1{:}10$ merger, so that the cooling time is $\sim$5 Gyr and the CC is soon restored.

These findings demonstrate that radiative cooling dominates the final ICM core properties, with physical processes governed by time-scales much shorter than those set by diffusion (Biffi & Valdarnini 2015).

To summarize, the results of this section demonstrate that the final level of core entropy, and thus the resiliency of CCs to disruption, depends critically on the merging mass ratio and initial orbit. Specifically, CCs are destroyed in head-on high-mass mergers, but can survive low-mass mergers or off-axis low mass ratio mergers. This suggests that the merging AM is a key parameter which determines the final remnant core entropy. In merging systems with high AM, a CC is re-established after the final collision as long as the cooling time is shorter than the core free-fall time. This condition depends on the merging mass ratio as well.

Our results are, partially, in agreement with Hahn et al. (2017). The authors argue that AM is a fundamental quantity to determine whether a CC can survive a cluster merger or not. They found CC disruption to occur in major mergers with low AM, but it is absent if the AM is high. This is in contrast with our findings, for which the disruption of CC in major mergers (mass ratio higher than 1:5) of massive clusters (i.e. with a primary mass $M_1 \gtrsim 6 \times 10^{14}\,\mathrm{M_\odot}$) occurs regardless of whether the merging is head-on or off-axis. Note also that the CC is not disrupted, and the AM becomes unimportant, when the primary mass is small ($M_1 \lesssim 10^{14}\,\mathrm{M_\odot}$).

Finally, our findings are in contrast with those of Z11. For the same set of merging initial conditions, that paper finds final levels of core entropy high enough to erase CCs, regardless of the considered merging case. This is at variance with the results of this section, in which the merging simulations now include gas cooling. This shows that a realistic physical modelling of the simulations is crucial to address the issue of CC survival in merging clusters.

4 CONCLUSIONS

In this paper, we have presented results extracted from a suite of idealized binary cluster merger simulations, realized using an *N*-body/hydro code which employs an improved SPH scheme. Each merging cluster simulation was performed by constructing two isolated gas+DM haloes in equilibrium; initial positions and velocities of the haloes are then assigned according to the specific orbital trajectory. We purposely adopted the same range of initial mass ratios and impact parameters as in a previous paper (Z11), so as to consistently compare our results with previous findings.

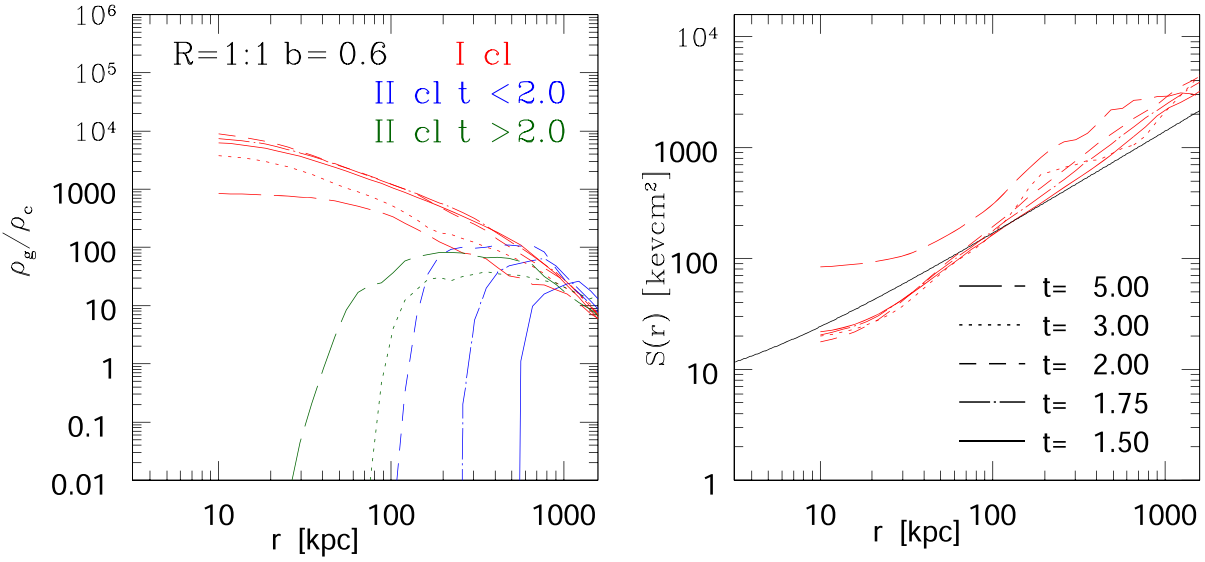

Figure 20. As in Fig. 12, we show here the gas density and entropy radial profiles for the $R = 1{:}1$ off-centre merger with $b = 0.6$. At variance with the run of Fig. 12, the simulation here incorporates radiative cooling.

Our simulations are aimed at investigating how the heating of the gas core leads to an increase of its entropy and to the disruption of the original CC profile during cluster mergers. In order to assess the impact of different physical processes on the survival of CC systems, we consider adiabatic as well as radiative merging simulations. The latter incorporate cooling, star formation, and supernovae feedback. Our main conclusions can be summarized as follows.

(i) For adiabatic simulations and head-on mergers, the dominant source of entropy is the shocking of the gas at the epoch of the first collision, with core heating being later driven by mixing processes.

(ii) In the case of off-axis mergers, core heating depends critically on the initial merging mass ratio, as well as on the angular momentum (AM) of the system. For equal-mass mergers part of the final core entropy owes its origin to the transfer of AM, induced by tidal torques occurring during the first encounter of the two clusters along their orbit. The corresponding increase in the primary circular velocity at this epoch (see Section 3.3) generates instabilities in the cluster inner regions, and in turn an increase in its core entropy.

(iii) For mergings with low mass ratios, the previous effect is negligible or absent and the bulk of core heating occurs at late stages, when the secondary accretes on to the primary. The final increase in core entropy can be modest because, before the final merging with the primary, most of the secondary mass has been stripped along its orbit by instabilities and ram pressure.

(iv) In general, our results from adiabatic simulations are in accord with previous findings (Z11). The initial CC profiles do not survive the various merger cases we considered, and because of the different physical processes occurring during cluster merging, high-entropy gas is always present in the cluster core after the merger.

(v) From a numerical point of view, it worth noting that the good hydrodynamical behaviour of the ISPH code presented here. For a specific run (see Fig. 9), we find the final entropy profile in good accord with the corresponding one shown in Z11. This is a non-trivial result since it demonstrates how the ISPH scheme, based on a Lagrangian formulation, can be considered competitive with Eulerian-based AMR codes in terms of hydrodynamical performance.

The scenario outlined above changes in several respects when cooling is incorporated in the simulations. The most important differences are:

(i) The increase in core entropy during cluster merging is now counteracted in part by radiative cooling, thus leading to lower levels of final entropy in the cluster inner regions than in the corresponding adiabatic case. CCs are found to survive if the merger is only able to raise the central entropy to $S(0) \lesssim 80\,\mathrm{keV\,cm^2}$. This implies that the cooling time is shorter than the Hubble time and the CC is restored.

(ii) For high mass mergers, CCs are destroyed in major merger, but are resilient to off-axis mergers with low mass ratios. This suggests that the survival of CCs depends both on the initial mass ratio and AM, and is thus characterized by a two-parameter dependence. This can be considered as the most important result of this paper.

(iii) Finally, this dependence on AM tends to disappear as one considers low-mass cluster mergers. We ran a head-on merger with a primary mass an order of magnitude smaller ($M_{200} = 6 \times 10^{13}\,\mathrm{M_\odot}$) than in the baseline simulations, and the final core entropy is found to be low and cooling dominated.

Overall, these findings support the observational evidence (Pratt et al. 2010; Chon et al. 2012) of a correlation between the CC/NCC core morphology and cluster mergers (but see Barnes et al. 2018, for a different viewpoint). The results presented here are also in broad agreement with previous works (Ritchie & Thomas 2002; Burns et al. 2008; Poole et al. 2008; Hahn et al. 2017), aimed at investigating the impact of merging clusters on core properties.

In particular Hahn et al. (2017) argued that CCs can survive major mergers with large AM. While our merging simulations also clearly indicate a significant role of AM in determining the status of the final core remnant, for the considered merging case we find that CCs are destroyed in high mass major mergers even in the case of large AM. We suggest that this discrepancy is not significant and is of statistical origin. Our results are obtained from binary cluster mergers realized in isolation with specific initial conditions, whereas the Hahn et al. (2017) sample is comprised of only ten clusters extracted from a previous cosmological simulation.

A possibility which has been left open by our study of merging clusters occurs when the merger is between an NCC and a CC cluster. In such a case, if the CC of the secondary is able to survive the merger process, it might settle in the centre of the primary, leading to a transition of the primary from an NCC to a CC state. However, we argue that this scenario is unlikely to occur.

This is justified by the chosen initial condition set up of our merger simulations, in which both the primary and the secondary are initialized as CC clusters. Our previous findings indicate that the CC of the secondary does not survive ram pressure and shock heating as it enters the atmosphere of the primary, regardless of the initial mass ratio and AM of the binary system. This result is valid for a primary CC cluster, but we expect it to be little affected by the level of core entropy of the primary.

The validity of our simulation results depends both on the numerical resolution of our simulations as well as on the adopted physical modelling of the gas. For several merging runs, in Section 3.2 we contrasted the final entropy profiles against parent merging simulations performed using a higher resolution. The stability of the corresponding profiles is shown in Fig. 9, indicating that our simulations can be considered free of resolution effects and are numerically converged.

In our simulations, the physical modelling of the ICM is based on a number of simplifying assumptions. In particular, the most relevant is the absence of a subgrid model for the energy injection from AGNs, which can offset radiative cooling in cluster cores. For the purpose of the present investigation, it is then important to assess the impact of AGN feedback on the results presented in Section 3.4.

Rasia et al. (2015) argued that CC thermal properties are affected by AGN feedback, and that its absence renders CCs more resilient against late-time mergers. This is in contrast with the findings of Hahn et al. (2017), for whom CC stability is not affected by incorporating AGN feedback, regardless of the adopted feedback parameters.

Hahn et al. (2017) suggest that this discrepancy is directly connected to the hydrodynamic codes used in the two sets of simulations. The authors performed their simulations using an Eulerian AMR code, while Rasia et al. (2015) employed an improved SPH scheme (see Sembolini et al. 2016). Hahn et al. (2017) argued that the treatment of thermal diffusion in the two codes is critical in determining thermal properties of the simulated CCs.

This topic has been discussed at length in Section 3.2 and, as mentioned in point (v) above, there is a full consistency between the final entropy profile of our $R = 1{:}1$ $b = 0$ merging simulation with the parent one of Z11. This strongly suggests that the artificial diffusion parameters of our hydrodynamical scheme are correctly calibrated. We thus assume that the inclusion of AGN feedback in radiative merging simulations will mirror the thermal behaviour of ICM seen by Hahn et al. (2017), and in turn should be of limited impact on the findings of Section 3.4.

However, the entropy profile of the head-on low-mass radiative merger depicted in the left-hand panel of Fig. 19 clearly exhibits an overcooling behaviour in its inner regions. Incorporating thermal AGN feedback in this simulation will avoid runaway cooling and will bring the final level of core entropy to higher values. Without a dedicated simulation including AGN feedback, it is difficult to assess the fate of the CC at the end of this merger.

From the parameters of cluster C3 ($M_{200} = 6 \times 10^{13}\,\mathrm{M}_{\odot}$) given in Table 1 and the entropy profile (24), we estimate an initial entropy value of $\simeq 12\,\mathrm{keVcm}^2$ at $r = 10\,\mathrm{kpc}$. Assuming that AGN feedback during the collision will maintain the core entropy of the primary at approximately this level, we require that the gain in core entropy be limited to $\lesssim 50 - 60\,\mathrm{keV\,cm}^2$ during the collision to keep the integrity of the CC. In this case, we expect the final central entropy level of the merger remnant to be below the CC threshold ($\simeq 80\,\mathrm{keV\,cm}^2$) previously given.

An upper limit to the level of core entropy achieved by the primary during the collision can be inferred by looking at the adiabatic merging simulation. From Fig. 19, we obtain a final core entropy $\simeq 100\,\mathrm{keV\,cm}^2$, but in the radiative simulations cooling effects will reduce this level to lower values. We thus conclude that for this specific merging case, the inclusion of thermal AGN feedback will change the ICM thermal state of the core. The final level of core entropy is likely to be close to the threshold above which the CC will be destroyed.

To summarize, our findings support the scenario in which the observed CC/NCC dichotomy is driven by cluster mergers. The difference in the disruption histories of the CCs, between adiabatic and radiative merging simulations, demonstrates that a realistic modelling of ICM physics is crucial in order to properly investigate the behaviour of core morphology during the merging phase. We argue that the inclusion in our simulations of AGN thermal feedback is unlikely to impact most of our findings, at least in merging simulations in which the final cluster remnant has a virial mass $M_{200} \gtrsim 6 \times 10^{14}\,\mathrm{M}_{\odot}$.

However, it must be stressed that in our high mass merging simulations, CCs survive only in mergers with low mass ratios and high AM. This leaves open the problem if such a result is consistent with the observed fraction of CC/NCC clusters at the present epoch (Barnes et al. 2018).

This issue can only be addressed in a cosmological framework, in which the evolution of simulated clusters can be followed self-consistently in a cosmological volume. Our idealized merging simulations are performed in isolation, so that environment effects are absent. In a cosmological simulation, these effects are automatically taken into account, and one expects merging environments to be affected.

On the other hand, our results indicate that the majority of core heating occurs when the secondary enters the innermost regions of the primary cluster. We thus suggest that environmental effects will be of limited impact on our findings.

ACKNOWLEDGEMENTS

RV gratefully acknowledges JA ZuHone for clarifying comments on the setup of the initial conditions described in Section 2.2. CLS was supported in part by NASA *Chandra* Grants GO7-18122X and GO8-19106X. The computations of this paper were carried out using the Ulisse cluster at SISSA and the Marconi cluster at CINECA (Italy), under a SISSA-CINECA agreement.

DATA AVAILABILITY

The data underlying this article will be shared on reasonable request to the corresponding author.

REFERENCES

Agertz O. et al., 2007, MNRAS, 380, 963
Arth A., Donnert J., Steinwandel U., Böss L., Halbesma T., Pütz M., Hubber D., Dolag K., 2019, preprint (arXiv:1907.11250)
Balsara D., 1995, J. Comput. Phys., 121, 357
Barnes D. J. et al., 2018, MNRAS, 481, 1809
Beck A. M. et al., 2016, MNRAS, 455, 2110
Bekki K., Owers M. S., Couch W. J., 2010, ApJ, 718, L27

Biffi V., Valdarnini R., 2015, MNRAS, 446, 2802
Binney J., Tremaine S., 1987, Galactic Dynamics. Princeton Univ. Press, Princeton
Buote D. A., 2002, in Feretti L., Gioia I. M., Giovannini G., eds, Astrophysics and Space Science Library, Vol. 272, Merging Processes in Galaxy Clusters. Kluwer Academic Publishers, Dordrecht, p. 79
Burns J. O., Hallman E. J., Gantner B., Motl P. M., Norman M. L., 2008, ApJ, 675, 1125
Cavagnolo K. W., Donahue M., Voit G. M., Sun M., 2009, ApJS, 182, 12
Chon G., Böhringer H., Smith G. P., 2012, A&A, 548, A59
Cullen L., Dehnen W., 2010, MNRAS, 408, 669
Diehl S., Rockefeller G., Fryer C. L., Riethmiller D., Statler T. S., 2015, Publ. Astron. Soc. Austr., 32, e048
Donnert J. M. F., 2014, MNRAS, 438, 1971
Donnert J. M. F., Beck A. M., Dolag K., Röttgering H. J. A., 2017, MNRAS, 471, 4587
Drakos N. E., Taylor J. E., Benson A. J., 2017, MNRAS, 468, 2345
Feretti L., Giovannini G., Govoni F., Murgia M., 2012, A&AR, 20, 54
Fujita Y., Takizawa M., Nagashima M., Enoki M., 1999, PASJ, 51, L1
García-Senz D., Cabezón R. M., Escartín J. A., 2012, A&A, 538, A9
Gastaldello F., Buote D. A., Humphrey P. J., Zappacosta L., Bullock J. S., Brighenti F., Mathews W. G., 2007, ApJ, 669, 158
Ghirardini V. et al., 2019, A&A, 621, A41
Gómez P. L., Loken C., Roettiger K., Burns J. O., 2002, ApJ, 569, 122
Groener A. M., Goldberg D. M., Sereno M., 2016, MNRAS, 455, 892
Hahn O., Martizzi D., Wu H.-Y., Evrard A. E., Teyssier R., Wechsler R. H., 2017, MNRAS, 470, 166
Halbesma T. L. R., Donnert J. M. F., de Vries M. N., Wise M. W., 2019, MNRAS, 483, 3851
Herant M., 1994, Mem. Soc. Astron. Ital., 65, 1013
Hopkins P. F., 2015, MNRAS, 450, 53
Johnson R., Ponman T. J., Finoguenov A., 2009, MNRAS, 395, 1287
Kazantzidis S., Magorrian J., Moore B., 2004, ApJ, 601, 37
Kim S. Y., Peter A. H. G., Wittman D., 2017, MNRAS, 469, 1414
Kuijken K., Dubinski J., 1994, MNRAS, 269, 13
Landau L. D., Lifshitz E. M., 1980, Statistical Physics, 3d edn. Pergamon, Oxford
Machado R. E. G., Lima Neto G. B., 2013, MNRAS, 430, 3249
McCarthy I. G. et al., 2007, MNRAS, 376, 497
McDonald M. et al., 2013, ApJ, 774, 23
Mansheim A. S. et al., 2017, MNRAS, 469, L20
Markevitch M., Vikhlinin A., 2007, Phys. Rep., 443, 1
Markevitch M., Gonzalez A. H., Clowe D., Vikhlinin A., Forman W., Jones C., Murray S., Tucker W., 2004, ApJ, 606, 819
Mastropietro C., Burkert A., 2008, MNRAS, 389, 967
Mitchell N. L., McCarthy I. G., Bower R. G., Theuns T., Crain R. A., 2009, MNRAS, 395, 180
Molnar S., 2016, Front. Astron. Space Sci., 2, 7
Molnar S. M., Broadhurst T., 2018, ApJ, 862, 112
Molnar S. M., Hearn N. C., Stadel J. G., 2012, ApJ, 748, 45
Monaghan J. J., 1997, J. Comput. Phys., 136, 298
Monaghan J. J., Price D. J., 2006, MNRAS, 365, 991
Nagasawa M., Nakamura T., Miyama S. M., 1988, PASJ, 40, 691
Navarro J. F., Frenk C. S., White S. D. M., 1997, ApJ, 490, 493
Pakmor R., Edelmann P., Röpke F. K., Hillebrand t W., 2012, MNRAS, 424, 2222
Planelles S., Quilis V., 2009, MNRAS, 399, 410
Poole G. B., Fardal M. A., Babul A., McCarthy I. G., Quinn T., Wadsley J., 2006, MNRAS, 373, 881
Poole G. B., Babul A., McCarthy I. G., Sand erson A. J. R., Fardal M. A., 2008, MNRAS, 391, 1163
Power C., Read J. I., Hobbs A., 2014, MNRAS, 440, 3243
Pratt G. W. et al., 2010, A&A, 511, A85
Price D. J. et al., 2018, Publ. Astron. Soc. Austr., 35, e031
Price D. J., 2008, J. Comput. Phys., 227, 10040
Price D. J., 2012, J. Comput. Phys., 231, 759
Price D. J., Monaghan J. J., 2007, MNRAS, 374, 1347
Rasia E. et al., 2015, ApJ, 813, L17
Raskin C., Owen J. M., 2016, ApJ, 820, 102
Read J. I., Hayfield T., 2012, MNRAS, 422, 3037
Reinhardt C., Stadel J., 2017, MNRAS, 467, 4252
Ricker P. M., Sarazin C. L., 2001, ApJ, 561, 621
Ritchie B. W., Thomas P. A., 2002, MNRAS, 329, 675
Robertson A., Massey R., Eke V., 2017, MNRAS, 465, 569
Roediger E., Bruggen M., Owers M. S., Ebeling H., Sun M., 2014, MNRAS, 443, L114
Roettiger K., Burns J. O., Loken C., 1996, ApJ, 473, 651
Rosswog S., 2015, MNRAS, 448, 3628
Rosswog S., Price D., 2007, MNRAS, 379, 915
Saitoh T. R., Makino J., 2016, ApJ, 823, 144
Sarazin C. L., 2002, in Feretti L., Gioia I. M., Giovannini G., eds, Astrophysics and Space Science Library, Vol. 272, Merging Processes in Galaxy Clusters. Kluwer Academic Publishers, Dordrecht, p. 1
Schmidt W., Byrohl C., Engels J. F., Behrens C., Niemeyer J. C., 2017, MNRAS, 470, 142
Sembolini F. et al., 2016, MNRAS, 457, 4063
Soker N., 2016, New Astron. Rev., 75, 1
Springel V., 2010, MNRAS, 401, 791
Springel V., Farrar G. R., 2007, MNRAS, 380, 911
Stroe A., Sobral D., Paulino-Afonso A., Alegre L., Calhau J., Santos S., van Weeren R., 2017, MNRAS, 465, 2916
Subramanian K., Shukurov A., Haugen N. E. L., 2006, MNRAS, 366, 1437
Sun M., Voit G. M., Donahue M., Jones C., Forman W., Vikhlinin A., 2009, ApJ, 693, 1142
Takizawa M., 2005, ApJ, 629, 791
Teyssier R., 2002, A&A, 385, 337
Turner J. A., Chapman S. J., Bhattal A. S., Disney M. J., Pongracic H., Whitworth A. P., 1995, MNRAS, 277, 705
Valdarnini R., 2006, New Astron., 12, 71
Valdarnini R., 2012, A&A, 546, A45
Valdarnini R., 2016, ApJ, 831, 103 (V16)
Valdarnini R., 2019, ApJ, 874, 42
Vazza F., Roediger E., Brüggen M., 2012, A&A, 544, A103
Vela L. V., Sanchez R., Geiger J., 2018, Computer Physics Communications, 224, 186
Vietri M., Ferrara A., Miniati F., 1997, ApJ, 483, 262
Vitvitska M., Klypin A. A., Kravtsov A. V., Wechsler R. H., Primack J. R., Bullock J. S., 2002, ApJ, 581, 799
Voit G. M., 2005, Rev. Mod. Phys., 77, 207
Wadsley J. W., Veeravalli G., Couchman H. M. P., 2008, MNRAS, 387, 427
Wang J., White S. D. M., 2007, MNRAS, 380, 93
Zemp M., Moore B., Stadel J., Carollo C. M., Madau P., 2008, MNRAS, 386, 1543
Zhang C., Yu Q., Lu Y., 2014, ApJ, 796, 138
Zhang C., Yu Q., Lu Y., 2015, ApJ, 813, 129
Zhang C., Yu Q., Lu Y., 2018, ApJ, 855, 36
ZuHone J. A., 2011, ApJ, 728, 54 (Z11)
ZuHone J. A., Ricker P. M., Lamb D. Q., Karen Yang H. Y., 2009, ApJ, 699, 1004
ZuHone J. A., Markevitch M., Johnson R. E., 2010, ApJ, 717, 908
ZuHone J. A., Zavala J., Vogelsberger M., 2019, ApJ, 882, 119
Zurek W. H., Benz W., 1986, ApJ, 308, 123

This paper has been typeset from a TEX/LATEX file prepared by the author.